

Quantifying degradation of the Imja Lake moraine dam with fused InSAR and SAR feature tracking time series

George Brencher¹, Scott T. Henderson^{2,3}, David E. Shean¹

5 ¹University of Washington Department of Civil and Environmental Engineering, 1400 NE Campus Parkway, Seattle, WA 98195, USA

²University of Washington Department of Earth and Space Sciences, 1707 NE Grant Lane, Seattle, WA 98195, USA

³University of Washington eScience Institute, 1410 NE Campus Parkway, Seattle, WA 98195, USA

Correspondence to: George Brencher (gbrench@uw.edu)

10 **Abstract.** Glacial lake outburst flood (GLOF) hazards are often tied to the structural properties of the moraines that dam glacial lakes. Traditional investigations of moraine dam structure and degradation involve costly and logistically challenging in situ geophysical and repeat topographic surveys, which can only be performed for a small number of sites. We developed a scalable satellite remote sensing approach using interferometric synthetic aperture radar (InSAR), InSAR coherence, and SAR feature tracking to precisely measure moraine dam surface displacement and map the extent of buried ice. We combined time series
15 from ascending and descending Sentinel-1 orbits to investigate vertical and horizontal surface displacement from 2017-2024 with ~12-day temporal sampling.

20 We applied our approach to quantify degradation of the Imja Lake moraine dam in the Everest Region of Nepal. We validated our SAR-based displacement measurements using 3D displacement measurements from very-high-resolution satellite stereo digital elevation models that span the study period. We found that a 0.3 km² area of the moraine dam has cumulatively subsided ~90 cm over the 7-year study period. Seasonal change in InSAR coherence provides evidence for buried ice throughout the moraine dam. We observed consistent downward and eastward displacement throughout the colder months, which we attribute to ice flow. The magnitude of downward vertical surface velocity increases in the warmer months, likely due to melting of buried ice. Our observations provide new insights into the timing and magnitude of the processes that control moraine dam
25 evolution, with broader implications for regional GLOF hazard assessment and mitigation.

1 Introduction

Glaciers in High Mountain Asia (HMA), Earth's largest glacierized region outside the poles, are expected to lose between ~29% and 67% of their total mass by the end of the century (Hock et al., 2019; Rounce et al., 2020). Worldwide, glacier thinning and retreat is associated with an increase in the formation of glacial lakes (Shugar et al., 2020). These lakes constitute
30 a significant hazard, as they can drain in sudden, catastrophic glacier lake outburst flood (GLOF) events that flood downstream valleys and can result in loss of life and damage to infrastructure (Mool et al., 2011; Riaz et al., 2014; Carrivick & Tweed,

Deleted: dammed by unstable ice-cored moraines

2016). For example, the September 2023 GLOF event in Sikkim, India, destroyed the Teesta III hydroelectric dam, washed away 15 bridges, stranded 3,000 tourists, and left at least 74 dead with more missing (Ali Badal, 2023; Choudhury & Hussain, 35 Kumar & Travelli, 2023; Sebastian, 2023).

Effective management of GLOF hazards involves 1) identification and monitoring of glacial lakes that pose a significant hazard, and 2) mitigation of this hazard before GLOFs occur, potentially through engineering solutions. The former has been primarily accomplished through hazard assessments ranging from a single lake (e.g. Budhathoki et al., 1970; Rana et al., 2000; 40 Wang et al., 2018; Sattar et al., 2021) to regional scale (e.g. Mool et al., 2011; Wang et al., 2012; Fujita et al., 2013; Allen et al., 2016; Rounce et al., 2017). Glacial lakes can be dammed by moraines, bedrock, and glacier ice (Rick et al., 2022). Where glacial lakes are dammed by moraines, hazard assessments frequently consider moraine dam stability, [the presence of buried ice within moraine dams](#), potential GLOF triggering events, and downstream impacts (Rounce et al., 2016). Where moraine dam instability is not identified as a primary GLOF trigger mechanism, melting of buried ice can increase lake area, reduce 45 width and height of dams, and provide potential pathways for seepage and piping (Richardson & Reynolds, 2000; Emmer & Cochachin, 2013; [Medeu et al., 2022](#)). As such, the evolution of moraine dams may substantially increase GLOF likelihood.

As glacial lakes, moraine dams, and the surrounding landscape change over time (Huggel et al., 2010; Shugar & Clague, 2011; Kellerer-pirklbauer et al., 2012; Ravanel et al., 2018), hazard assessment and mitigation tasks require repeated observations 50 (Fujita et al., 2009; Rounce et al., 2017; Emmer et al., 2018). Satellite remote sensing has been used to create glacial lake inventories, track glacial lake development (e.g. Fujita et al., 2009; Nie et al., 2018; Shugar et al., 2020), and recently, to monitor glacial lake dam and bank evolution (Haritashya et al., 2018; Scapozza et al., 2019; [Wangchuk et al., 2022](#); Yang et al., 2022; Jiang et al., 2023; Yang et al., 2023; Yu et al., 2024). These remote measurements of surface displacement can be used to assess moraine dam stability, infer moraine dam structure, and quantify changes in moraine dam topography, providing 55 critical information for GLOF hazard assessments and potentially guiding prioritization for in-situ surveys and hazard mitigation strategies.

1.2 Remote sensing of moraine dam degradation

C-band SAR can operate during both day or night, penetrate through clouds, and penetrate thin, dry snow (Bürgmann et al., 2000; Sun et al., 2015). Both InSAR and SAR feature tracking (of images in original range-azimuth coordinates) can provide 60 measurements of surface motion in the radar line-of-sight (LOS) direction.

InSAR relates the phase offset from successive SAR acquisitions to surface displacement, potentially with mm-level accuracy (Bürgmann et al., 2000; Rosen et al., 2000). InSAR has frequently been applied to measure displacement of ice-rich features, including glaciers and ice sheets (Massonnet & Feigl, 1998; Rosen et al., 2000), rock glaciers (Bertone et al., 2022), and

Deleted: GLOFs can be triggered by rockfall, landslides, avalanches, glacier calving, precipitation and snowmelt events, a failure of the dam (Costa & Schuster, 1988; Richardson and Reynolds, 2000a; Neupane et al., 2019).

Deleted: a

Deleted: ¶

Deleted: ¶

Here, we present a new method that leverages time series of synthetic aperture radar (SAR) images to precisely measure moraine dam surface movement over the past decade. We used this new approach to characterize moraine dam kinematics and improve understanding of processes contributing to the Imja Lake moraine dam evolution in the Everest region of Nepal.

Deleted: 1.1 Moraine dam evolution¶

Ice-cored moraines are found globally in modern glacier forelands (Østrem, 1959). These features, which range in size from the decameter to kilometer scale, are typically formed at glacier margin when ice overlain by insulating debris cover is disconnected from the active glacier through differential ablation (Østrem, 1959; Kjær & Krüger, 2001; Lukas, 2011). Ice-cored moraines often impound meltwater to form proglacial glacial lakes, becoming moraine dams.

Once cut off from the active upstream glacier, ice-cored moraine dam degradation proceeds through multiple related processes, which change the topographic and structural characteristics of moraine dams over time. Understanding these mechanisms is important for both method development and interpretation of surface displacement measurements from remote sensing observations. Several processes contribute to degradation of ice-cored moraines, including 1) downwasting, 2) thermokarst, 3) backwasting, and 4) debris reworking.

Downwasting, or vertical subsidence of ice-cored features, occurs due to melting and sublimation of buried ice (Lukas, 2011). Downwasting rates have been observed to vary between 0.003 and 4.8 m/yr, and spatiotemporal variability is correlated with mean annual temperature and debris thickness (Irvine-Fynn et al., 2011). The downwasting rate of ice-cored moraine dams may have significant implications for GLOF hazards, as it relates directly to changes in the freeboard height of the dam and the shape of the shoreline, leading to lake expansion.

Thermokarst occurs where melting of glacial ice or ground ice beneath unconsolidated sediments creates pseudokarst landforms including kettles and sinkholes (Healy, 1975). Thermokarst landforms may contribute to rapid surface lowering, as melting of buried ice is accelerated by the presence of liquid water (Richardson & Reynolds, 2000b). Remnant glacial structures including water- and debris-filled crevasses likely exert a primary control over thermokarst landform location (Richardson & Reynolds, 2000b).

Backwasting, or lateral retreat of near-vertical ice walls and ice-cored slopes, is the dominant ice loss mechanism for most ice-cored moraines (Krüger & Kjær, 2000; Lukas, 2011). Unlike downwasting, backwasting rates are primarily controlled by local

Deleted: ¶

We propose a novel approach to combine C-band (~5 cm wavelength) InSAR and SAR feature tracking to measure displacement of moraine dams and distinguish between various physical degradation processes.

permafrost (Zhang et al., 2022). Recently, InSAR has also been applied to quantify surface movement of glacial lake dams (Scapozza et al., 2019; Yang et al., 2022; Jiang et al., 2023; Yang et al., 2023; Yu et al., 2024).

840 While InSAR offers unparalleled precision, several factors can reduce measurement accuracy, including atmospheric noise, layover, and radar shadow. InSAR requires 1) coherent surface change with similar scatterer characteristics between radar acquisitions, and 2) LOS surface displacement of less than half the radar wavelength (2.8 cm for C-band) between adjacent pixels (Itoh, 1982; Handwerger et al., 2015). While errors caused by atmospheric conditions and acquisition geometry can be avoided or corrected, errors caused by rapid surface change may cause underestimation of true LOS surface velocity. InSAR 845 coherence, a unitless measure of the “sameness” of surface scatterers between acquisitions, can be used to discriminate between reliable and unreliable InSAR measurements (e.g. Schmidt & Bürgmann, 2003). InSAR coherence can also be used to identify significant change in surface characteristics, and low coherence has been used to map the extent of desert erosion (e.g. Cabré et al., 2020), landslides (e.g. Ohki et al., 2020; Jacquemart and Tiampo, 2021), flooding (e.g. Chini et al., 2019), and debris-covered glaciers (e.g. [Atwood et al., 2010](#); [Frey et al., 2012](#); Lippl et al., 2018).

850

Feature tracking (pixel offset) techniques offer an alternative method to retrieve surface displacement measurements from SAR data when InSAR is not possible due to loss of coherence or large displacement gradients between adjacent pixels. Feature tracking involves 2D cross-correlation of backscatter amplitude values in successive radar images to measure offsets in the range (across-track) and azimuth (along-track) directions. This technique has been used to measure glacier surface velocity 855 (e.g. Fahnestock et al., 1993; Strozzi et al., 2002, 2008; Fahnestock et al., 2016) and fast-moving features surrounding glacial lakes (Scapozza et al., 2019; Yang et al., 2022). While feature-tracking measurements offer lower resolution and precision than InSAR measurements, and measurement quality can be degraded by large surface changes, they are more robust to large surface displacements and rapid surface change (Joughin, 2002, Zheng et al., 2023).

860 Here, we present a method to create a single cumulative displacement time series from InSAR and feature tracking measurements using a variation of the small baseline subset approach (SBAS; Berardino et al., 2002; Schmidt and Bürgmann, 2003). The SBAS approach uses a network of displacement observations to solve for the displacement of a given pixel between successive acquisitions. It was developed for InSAR interferograms (Berardino et al., 2002) and has subsequently been applied to SAR feature tracking (e.g., Casu et al., 2011; Euillades et al., 2016; Guo et al., 2020; Samsonov et al., 2021) and optical 865 feature tracking offsets (e.g., Bontemps et al., 2018; Altena et al., 2019; Lacroix et al., 2019). The SBAS approach, however, has issues during periods with poor coherence between successive acquisitions, which can introduce errors in the resulting displacement time series. This limitation has previously been addressed by constraining the time series inversion using geophysical constraints parameterized in time (López-Quiroz et al., 2009) and spatial covariance (Jolivet and Simons, 2018). We address this issue by constraining the per-pixel InSAR time series inversion with additional observations from SAR feature

870 tracking, which is more robust to decorrelation than InSAR. Our approach does not require prior assumptions about the displacement patterns of pixels over time.▼

▼ Previous studies combined InSAR and feature tracking to produce self-consistent surface displacement maps over large ice sheets and ice caps, where surface velocity is often too fast for InSAR alone (e.g., Joughin, 2002; Gray et al., 2007; Liu et al., 875 2007; Sánchez-Gámez & Navarro, 2017; Joughin et al., 2018). To our knowledge, no studies have combined these techniques to measure year-round surface displacement of ice-cored moraine features, where we expect seasonal variability in surface melt rates and associated debris reworking.

2 Imja Lake Study Site

880 Imja Lake is a ~2.8 by 0.6 km glacial lake covering ~1.6 km² in the Everest region of Nepal (Fig. 1). Imja Lake is impounded on its north and south sides by lateral moraines, above which rise the steep slopes of adjacent mountain peaks: Imja Tse to the north and Ombigaichen to the south. To the east, the ~860 m wide calving front of the Lhoste Shar and Imja Glaciers terminate in the lake. Imja Lake formed in the early 1970s as supraglacial lakes coalesced on the stagnant, debris-covered tongue of Imja Glacier. It expanded at a roughly linear rate of 0.02 km²/yr until 1997, then at a rate of 0.03 km²/yr from 1997 to 2020 (Watanabe et al., 2009; Gupta et al., 2023).

885

To the west, Imja Lake is impounded by an ice-cored terminal moraine covering 0.62 km². The Imja Lake moraine dam (hereafter, the moraine dam) has a low-relief hummocky surface with ridges and furrows, ponds, and ice cliffs, with a mean elevation of 4982 m (orthometric height above the EGM2008 geoid). The lake drains over the moraine via a series of linked ponds. An artificial drainage channel was constructed downstream of the western pond in 2016 (UNDP, 2012; Khadra, 2016). 890 The moraine dam has an enclosed concave-up surface, and broadly slopes down toward the lake and surface ponds (Fig. S1). Immediately northwest of the moraine dam is a lobe of the debris-covered Lhotse Glacier.

Deleted: 1

Deleted: By combining InSAR and feature tracking measurements, we can leverage the strengths of both methods to provide a more complete record and understanding of moraine dam kinematics. This approach captures large seasonal variations, including slow cold-season displacement with InSAR and rapid warm-season surface change with feature tracking. With that said, there are some trade-offs associated with this approach. Because feature tracking measures the displacement of discrete kernels of neighboring pixels, it provides inherently lower spatial resolution than per-pixel InSAR displacements (Joughin, 2002). By combining both InSAR and feature tracking measurements, we effectively degrade the spatial resolution of the InSAR measurements in exchange for improved displacement accuracy. This compromise is essential for applications involving debris-covered ice, when large surface change during the warmer months reduces InSAR coherence between Sentinel-1 acquisitions. It is also important to note that extreme, rapid and/or highly localized surface change from processes like iceberg calving, backwasting, and fast-moving debris flows will still present challenges for the combined approach, potentially resulting in underestimation of surface deformation. Nonetheless, combining InSAR and feature tracking offers improved displacement time series that are more accurate than time series produced independently using these two methods.¶

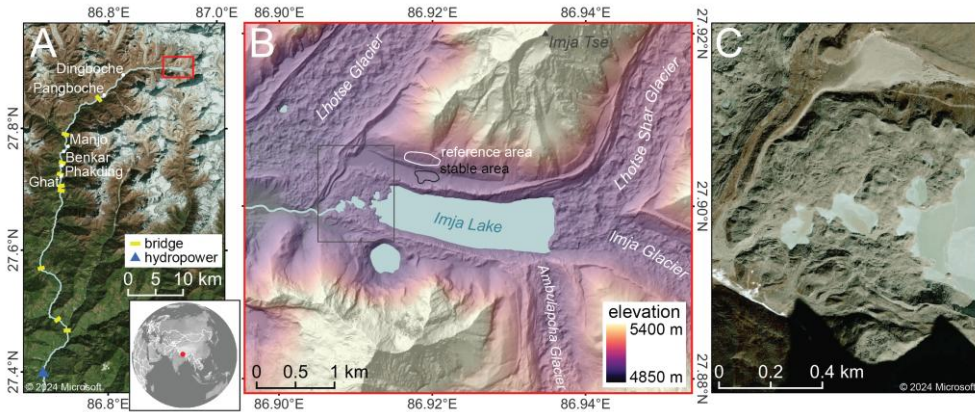


Figure 1: Context maps for the Imja Lake moraine dam. A) Microsoft satellite basemap showing the area downstream of Imja Lake, including settlements and infrastructure along the Dhudh Kohsi river. B) Color-shaded relief map from median composite of EarthDEM strips acquired during the 2014-2019 period (Porter et al., 2022). C) Microsoft satellite basemap detail of the Imja Lake moraine dam. Microsoft product screen shots reprinted with permission from Microsoft Corporation.

Geophysical studies using ground-penetrating radar (GPR) and electrical resistivity tomography (ERT) have documented the extent and thickness of buried ice in the moraine dam, with continuous buried ice tens of meters thick to the east transitioning to discontinuous blocks of buried ice to the west (Hambrey et al., 2008; Somos-Valenzuela et al., 2012; Dahal et al., 2018).

Two studies have quantified Imja Lake moraine dam degradation rates using in situ measurements obtained with traditional and Global Positioning System (GPS) surveying techniques (Watanabe et al., 1995; Fujita et al., 2009), and one study measured moraine dam displacement by differencing the 30-m Shuttle Radar Topographic Mission Global 1 (SRTM-GL1) DEM acquired in February 2000 with a 2-m WorldView stereo DEM acquired in February 2016 (Haritashya et al., 2018). These studies document meter- to sub-meter-scale subsidence and horizontal motion over the surface of the moraine dam, with the fastest motion occurring in the northeast area.

920

925

930 3 Data

We downloaded all available Copernicus Sentinel-1 C-band single-look complex (SLC) SAR images collected over the study site from January 1, 2017 through March 1, 2024. The revisit time for this period was generally 12 days, and we did not include data before 2017 due to longer gaps between acquisitions. All images were acquired in interferometric wide (IW) swath mode with vertical co-polarization (VV) along ascending (satellite moving north and looking east) relative orbit 12 and descending (satellite moving south and looking west) relative orbit 121. To minimize download time and storage, we limited processing to SLC bursts covering our study site, with a total of 214 ascending burst acquisitions (Burst ID 012_023790_IW1) and 227

descending burst acquisitions (Burst ID 121_258661_IW2). Burst dimensions are ~20 km in azimuth (along-track direction) by ~85 km in range (across-track direction) with pixel spacing of 14.1 m in azimuth and 2.3 m in range (Fig. S2).

940 We used the 2022_1 release of the 30-m Copernicus GLO-30 DEM (European Space Agency, 2021) to remove the topographic component of the phase and geocode the SAR data products. The GLO-30 DEM product has an absolute vertical accuracy (LE90) of <4 m and an absolute horizontal accuracy (CE90) of <6 m (NSDDA, 1998; European Space Agency, 2022).

945 We downloaded daily 2-m air temperature and total precipitation data from the Pyramid Weather Station (UCAR/NCAR-Earth Observing Laboratory et al., 2011), which is located ~11 km northwest of the Imja Lake moraine dam at an elevation of 4951 m, about 30 m lower than the elevation of the moraine dam. We aggregated available daily measurements between October 1, 2002 to December 31, 2009 to derive monthly climatology (mean, minimum, maximum and standard deviation) for the ~7-year period.

4 Methods

950 By combining InSAR and feature tracking measurements, we leverage the strengths of both methods to provide a more complete record and understanding of moraine dam kinematics. This approach captures large seasonal variations, including slow cold-season displacement with InSAR and rapid warm-season surface change with feature tracking. However, feature tracking measures the displacement of discrete kernels of neighbouring pixels, so it provides inherently lower spatial resolution than per-pixel InSAR displacements (Joughin, 2002). By combining both InSAR and feature tracking measurements, we effectively degrade the spatial resolution of the InSAR measurements in exchange for improved displacement accuracy. This compromise is essential for applications involving debris-covered ice, when large surface change during the warmer months reduces InSAR coherence between Sentinel-1 acquisitions. It is also important to note that extreme, rapid and/or highly localized surface change from processes like iceberg calving, backwasting, and fast-moving debris flows will still present challenges for the combined approach, potentially resulting in underestimation of surface deformation. Nonetheless, combining InSAR and feature tracking offers improved displacement time series that are more accurate than time series produced independently using these two methods.

Deleted: can

Formatted: Normal

Deleted: With that said, there are some trade-offs associated with this approach.

Deleted: Because

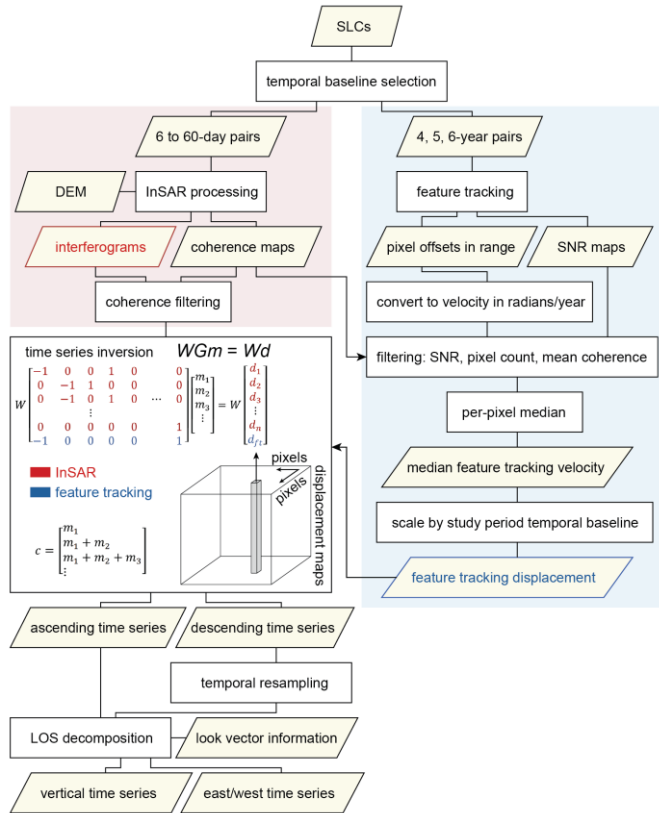
Deleted: neighboring

Deleted: ¶

4.1 SAR data processing

To extract surface displacement information from the Sentinel-1 SLC products, we generated both interferograms and feature tracking offsets using the Hybrid Pluggable Processing Pipeline (HyP3) ISCE2 Plugin (Hogenson et al., 2020), which enables 955 batch processing with the Jet Propulsion Laboratory InSAR Scientific Computing Environment (ISCE) software (Fig. 2; Rosen et al., 2012; version 2.6.3).

975 The insar_tops_burst workflow was used to process interferograms with five looks (effectively, a spatial averaging factor of five) in the range direction and one look in the azimuth direction, geocoded to 20 m square pixels (Fig. S2; Fig. S3). To form redundant networks of ascending and descending interferograms, we created interferograms for each burst acquisition using the three nearest burst acquisitions in time. In total, we processed 636 ascending burst interferograms and 675 descending burst interferograms (Table 1).



980 **Figure 2: Flowchart illustrating our combined InSAR and feature-tracking approach. The time series inversion schematic is adapted from Schmidt and Bürgmann (2003). The equation relates the observed phase change (d) from each of n interferograms and a single cumulative feature tracking displacement product ($d_{f,l}$) to the change in phase between acquisitions (m) at a given pixel. The design matrix G describes the temporal baseline of each pair, with -1 corresponding to the primary acquisition date and 1 corresponding to the secondary acquisition date. The diagonal weight matrix W includes coherence values. The cumulative phase change time series (c) is prepared from the inversion results for each pixel.**

We selected a local “reference area” and “stable area” (Fig. 1) as close to the moraine dam as possible with high mean InSAR coherence for the entire study period. The reference area ($\sim 0.06 \text{ km}^2$, ~ 144 pixels) was used to remove atmospheric noise, 990 while the stable area ($\sim 0.03 \text{ km}^2$, ~ 87 pixels) was used to assess derived measurement accuracy and precision.

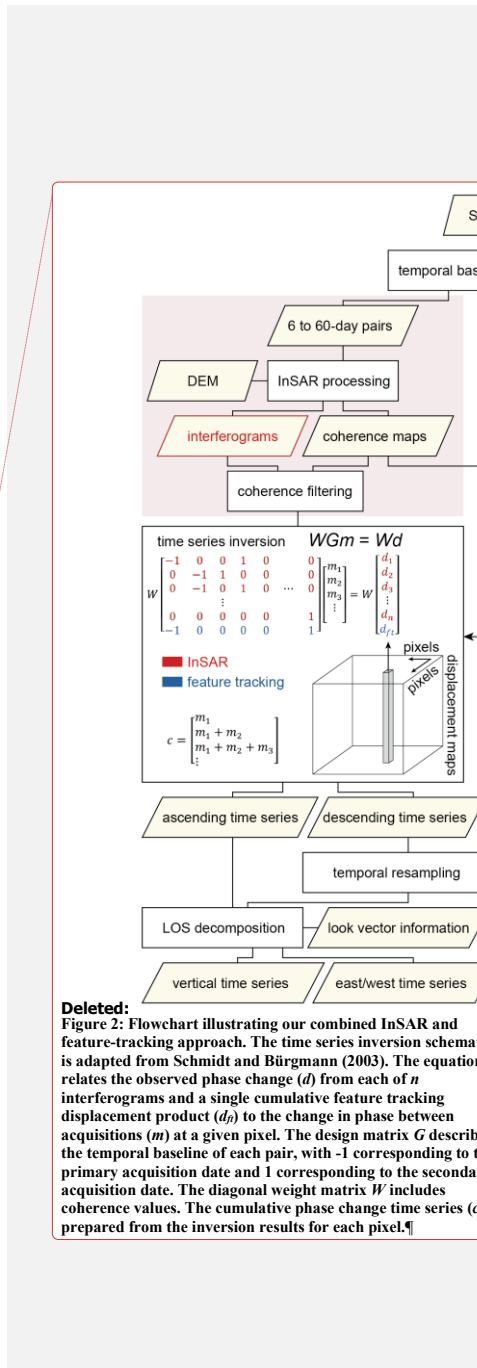
We co-registered all SLCs and performed feature tracking on the SLC products in radar coordinates at the native resolution using a modified version of the `insar_tops_burst` workflow and the ‘dense ampcor’ ISCE2 feature tracking routine (Fig. 2).

We selected kernel sizes and skip sizes based on the characteristics of the moraine dam and an empirical sensitivity analysis.

995 The moraine dam is roughly square (~ 800 by 900 m) in ground range. To maximize the number of unique feature-tracking measurements over the moraine dam that do not extend beyond the edge of the feature, we chose to use kernel sizes and skip sizes that were roughly square in ground range. Kernels that span the moraine dam and the surrounding area are likely to produce poor matches due to intra-kernel variability in the magnitude and direction of surface displacement.

1000 Smaller kernel sizes will result in poor matching, while larger kernel sizes will reduce the spatial resolution of the output feature tracking measurements. We found that a kernel size of 10 pixels in azimuth and 60 pixels in range, (141 by 138 m in ground range) was the smallest possible square kernel size that provided high-quality matches. We used a skip size of 4 pixels in azimuth and 20 pixels in range, or 56 by 46 m in ground range, to minimize interpolation without increasing processing time. Smaller skip sizes substantially increased processing time with negligible improvement, while larger skip sizes required 1005 more interpolation between sparse measurements. The search window size was set to 10 pixels in azimuth and 30 pixels in range, or 141 m by 69 m, much larger than the expected cumulative surface displacement of the moraine dam over the study period.

To estimate the accuracy of our feature tracking measurements, we first calculated the ground-range resolution of the slant-range SLCs. Following Notti et al., (2010) we computed the ratio of slant-range resolution to ground-range resolution (R-index) for the SLCs, considering terrain slope, terrain aspect, and the radar LOS vectors. We used this index to calculate the 1010 SLC resolution in the ground-range direction (Fig. S4). Over the moraine dam, the median ground-range resolution was 4.38 m for the ascending SLCs and 3.82 m for the descending SLCs. Assuming perfect SLC co-registration and a conservative feature-tracking precision of 0.2 pixels (Fialko & Simons, 2001; Strozzi et al., 2002), the theoretical accuracy of our feature 1015 tracking measurements is 2.82 m in azimuth, 0.88 m in range for the ascending SLCs, and 0.76 m in range for the descending SLCs. Given the expected mean surface velocity of <1 m per year for the moraine dam (Fujita et al., 2009), we generated feature tracking offsets with multi-year temporal baselines to maximize displacement between acquisitions. As longer temporal baselines could result in degraded quality due to significant changes in surface scatterer characteristics, we generated offsets for all possible feature tracking image pairs with temporal baselines of 4, 5, and 6 years (Table 1). In total, we generated 192 1020 ascending and 210 descending feature tracking offset maps with corresponding signal-to-noise ratio (SNR) maps. The expected



precision in the range direction for the 4-, 5-, and 6-year feature tracking offset maps is 0.22 m/yr, 0.18 m/yr, and 0.15 m/yr, 1035 respectively.

Table 1. Summary of InSAR and feature tracking datasets.

Orbit	Acquisitions	Dataset	Pair count	Mean temporal baseline	Temporal baseline range
ascending track 12, Burst ID 012_023790_IW1	214	InSAR	636	24.3 days	12-48 days
		feature tracking	192	4.7 years	4-6 years
descending track 121, Burst ID 121_258661_IW2	227	InSAR	675	23.0 days	6-60 days
		feature tracking	210	4.7 years	4-6 years

4.2 Time series inversion

Since both InSAR interferograms and the component of feature-tracking motion in the slant-range direction are measurements 1040 of displacement along the radar LOS (Fig. S5), these measurements can be combined to prepare more accurate estimates of LOS surface displacement over time. We used the Miami INsar Time-series software in PYthon (MintPy) package (Yunjun et al., 2019) to prepare cumulative LOS displacement time series from all InSAR and feature tracking observations for each relative orbit.

1045 To avoid cumulative displacement errors caused by poor feature tracking matches, we aggregated the available feature tracking offset products over time and prepared a single median velocity product for each relative orbit. These median velocity products were then used to constrain the cumulative displacement solution from the network of InSAR interferograms from the same relative orbit (Fig. 2).

1050 Several preprocessing steps were required to produce the median feature tracking velocity products for each relative orbit. We first converted all feature tracking offsets in range from pixels to C-band phase in radians, the same unit as our interferograms. We then masked all pixels with signal-to-noise ratio lower than 8 to remove unreliable measurements (Casu et al., 2011). This threshold was set to minimize the resulting magnitude of noise in the stable area. Next, we calculated the median surface displacement in range observed in the reference area and subtracted it from each offset map to mitigate potential co-registration 1055 bias. At this point we divided each feature tracking offset map in range by its temporal baseline and computed a per-pixel median rate for the entire time series stack, resulting in a single median velocity product for each relative orbit. We masked any pixels with less than 10 feature-tracking observations or a mean InSAR coherence greater than 0.85 during late summer (day of year 220–280, the lowest coherence period, Fig. 4), as the InSAR measurements alone should provide accurate displacement time series for those pixels. We also computed the per-pixel standard deviation of the feature tracking offset 1060 maps to assess variability due to real changes and measurement error.

Prior to time series inversion, we removed interferograms with mean coherence of less than 0.6 over the moraine dam, unless they were required to form a continuous network. This filter effectively removed interferograms impacted by intermittent snow accumulation, larger (>200 m) perpendicular baselines, or large surface change over the temporal baseline. To convert our per-pixel median feature tracking velocity (displacement rate) products into a cumulative displacement product analogous to an interferogram for the full 2017 to 2024 study period, we multiplied by the appropriate temporal baseline for the ascending (7.29 years) and descending (7.36 years) time series. The cumulative feature tracking displacement product was assigned a uniform coherence of 0.6, which is the minimum allowable mean coherence for the moraine dam area. The network of per-pixel displacement measurements, including the interferograms and the ~7-year cumulative feature tracking displacement product, was then inverted using phase variance, a measure of expected phase noise calculated using coherence (Tough et al., 1995; Hanssen et al., 2001), as a weight (Yunjun et al., 2019). As coherence is used to calculate phase variance, the cumulative feature tracking displacement product is weighted lower than interferograms where coherence is greater than 0.6.

Following the time series inversion, we computed and removed the median apparent displacement over the reference area from the LOS displacement estimate at each time step to mitigate atmospheric noise. The standard deviation of the median apparent displacement values over the reference area was 3.1 cm for the ascending data ($n=214$) and 0.5 cm for the descending data ($n=227$). The moraine dam is approximately 900 by 800 m and the reference area is only 250 m northwest of the moraine dam. Given the expected correlation length scales of several km for atmospheric noise in mountains (e.g., Bekaert et al., 2015), the apparent displacement in the reference area should be similar to the atmospheric noise over the moraine dam. To evaluate remaining measurement uncertainty, we first computed the mean apparent displacement in the stable area at each time step, then computed the standard deviation of this spatial mean over all time steps to characterize the magnitude of remaining atmospheric noise at a given time step. The standard deviation was 0.2 cm for the ascending orbit and 0.4 cm for the descending orbit. Finally, we delineated a “moving area” polygon over the moraine dam including pixels with mean velocity of ~1 cm/yr above the background noise level in the ascending and descending cumulative displacement time series.

1085 4.3 Surface displacement from LOS decomposition

Given two cumulative displacement measurements over the moraine dam, each with a different LOS from different relative orbits, we can solve for two components of the 3D surface displacement vector (Wright et al., 2004; Fuhrmann & Garthwaite, 2019). Since the mean LOS incidence angle at the site is 35.8° for the ascending burst and 37.8° for the descending burst, and the mean LOS azimuth (defined clockwise from north) is 79.3° for the ascending burst and 280.5° for the descending burst, we chose to solve for the vertical (up/down) and horizontal (east/west) surface displacement components. We assume that any north/south displacement would be negligible when projected into the available LOS vectors.

The LOS unit vector (\hat{l}) of each pixel can be defined as:

$$\hat{l} = \cos(\gamma) \sin(\theta) \hat{n} + \sin(\gamma) \sin(\theta) \hat{e} - \cos(\theta) \hat{z}, \quad (1)$$

1095 for ascending (\hat{l}_{asc}) and descending (\hat{l}_{des}) geometry, where γ is the LOS azimuth angle, θ is the LOS incidence angle defined relative to surface-normal direction, and \hat{n} , \hat{e} and \hat{z} represent the north, east, and up axes, respectively, which define the up/down $\hat{l}_{ud} = 0\hat{n} + 0\hat{e} + 1\hat{z}$ and east/west $\hat{l}_{ew} = 0\hat{n} + 1\hat{e} + 0\hat{z}$ unit vectors.

If we assume that the observed cumulative ascending ($d_{asc}(t)$) and descending ($d_{des}(t)$) displacement at time t is only
1100 sensitive to the up/down ($d_{ud}(t)$) and east/west ($d_{ew}(t)$) surface displacement components, we obtain the following equations:

$$d_{asc(t)} = \hat{l}_{asc} \cdot \hat{l}_{ud} * d_{ud}(t) + \hat{l}_{asc} \cdot \hat{l}_{ew} * d_{ew}(t), \quad (2)$$

$$d_{des(t)} = \hat{l}_{des} \cdot \hat{l}_{ud} * d_{ud}(t) + \hat{l}_{des} \cdot \hat{l}_{ew} * d_{ew}(t), \quad (3)$$

We can then rearrange these equations to solve for the up/down and east/west displacement components:

$$1105 d_{ud}(t) = \frac{\hat{l}_{asc} \cdot \hat{l}_{ew} * d_{des}(t) - \hat{l}_{des} \cdot \hat{l}_{ew} * d_{asc}(t)}{\hat{l}_{asc} \cdot \hat{l}_{ew} * \hat{l}_{des} \cdot \hat{l}_{ud} - \hat{l}_{des} \cdot \hat{l}_{ew} * \hat{l}_{asc} \cdot \hat{l}_{ud}}, \quad (4)$$

$$d_{ew}(t) = \frac{\hat{l}_{asc} \cdot \hat{l}_{ud} * d_{ud}(t) - d_{asc}(t)}{\hat{l}_{asc} \cdot \hat{l}_{ew}}, \quad (5)$$

To accomplish this, we interpolated the descending orbit cumulative displacement time series to match the acquisition dates of the ascending orbit cumulative displacement time series, and then solved for the vertical and east/west displacement at every pixel at each ascending acquisition time.

1110 To compute the vertical and east/west surface velocity, we divided the observed cumulative displacement by the time between acquisition dates. We aggregated these velocity component time series to compute the per-pixel monthly median values over the entire study period.

1115 To identify and map areas of buried ice, we calculated a winter coherence map using the per-pixel median coherence for all 12-day temporal baseline observations in winter to early spring (day of year 0–100), and a summer coherence map using the per-pixel median coherence for observations in late summer (day of year 220–280). We attribute large observed seasonal decreases in InSAR coherence to surface changes caused by melting of buried ice during warm months.

4.4 Preparation of a high-resolution 3D displacement validation dataset from stereo DEMs

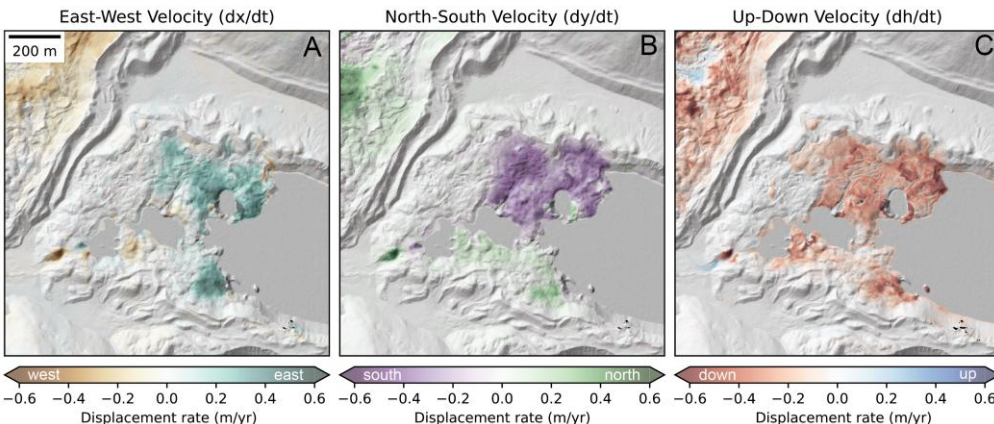
1120 We identified and processed two Maxar WorldView-3 in-track stereo image pairs spanning the 2017–2024 study period, including the February 11, 2016 WorldView-3 stereo pair (catalog IDs 104001001854B000, 10400100175C2D00) used by Haritashya et al. (2018), and a new in-track stereo pair acquired on January 30, 2025 (10400100A0D45D00,

10400100A193EE00). We used the latest version (3.5.0-alpha) of the Ames Stereo Pipeline (Shean et al., 2016; Beyer et al., 2018) and the processing settings outlined by Bhushan and Shean (2021) and Bhushan et al. (2024) to prepare the
1125 corresponding DEMs with 1-m posting.

We co-registered the January 30, 2025 DEM to the February 11, 2016 DEM using the demcoreg (Shean et al., 2023) implementation of the Nuth and Kääb (2011) algorithm (Fig. S6). We then corrected residual in-track “jitter” and cross-track “CCD array geometry” artifacts (see Shean et al., 2016) by fitting a Savitzky-Golay filter (window of 101 px, 2nd-order
1130 polynomial basis function) to median of elevation difference residuals over static surfaces for each row and column (Fig. S7; see `ct_at_correction_wrapper` function of `demcoreg/coreglib.py`).

We prepared final cumulative elevation change and elevation change rate maps for the ~9-year period (Fig. 3C). The final elevation difference residuals over all exposed static control surfaces used during co-registration had a median of 0.00 m and
1135 normalized median absolute deviation (NMAD) of 0.14 m (<0.5 px) for the ~9-year period (Fig. S8), corresponding to a 1-sigma uncertainty of ~1.6 cm/yr. The elevation difference residuals over the stable area used for calibration of the InSAR and feature-tracking results (see Fig. 1 for context) had a mean bias of -0.54 cm and a standard deviation of 7.77 cm, corresponding to apparent vertical displacement rates of -0.06 cm/yr and 0.87 cm/yr, respectively.

Validation Data: 3D Displacement Rates from WV-3 Stereo DEMs (2016-02-11 to 2025-01-30, 8.97 yr)



1140 Figure 3: Long-term (~9-year) east/west, north/south, and vertical surface velocity validation data, calculated from feature tracking
| of co-registered 1-m DEM hillshade products and a vertical DEM difference [product](#). These products document the spatial extent
| and magnitude of moraine dam surface motion during the study period with enough detail to capture signals associated with ice cliff
| retreat, downslope flow, and [anthropogenic](#) cut/fill and [sediment deposition](#) associated with the October 2016 lowering project
1145 (UNDP, 2012; Khadra, 2016). These products serve as validation for the combined InSAR and SAR feature-tracking time series,
which offer detailed temporal evolution of these processes (Figures 4-5), with reduced spatial resolution.

Deleted: ¶

Deleted: map

Deleted: downstream

Following co-registration, we created shaded relief maps for the two DEMs using the “combined” hillshade option in the
1150 gdaldem utility (Rouault et al., 2024). We digitized the lake and pond shoreline using the January 30, 2025 orthoimages and
shaded relief map, and masked the hillshade products over water. We then used the Ames Stereo Pipeline correlator
(*disp_mgm_corr.py* utility of Bhushan and Shean [2025]) to prepare dense horizontal sub-pixel displacement maps tracking
surface motion between the hillshade products, following the methods outlined in Bhushan et al. (2024). The final horizontal
velocity (m/yr) components (Fig. 3A–B) were calculated based on the 1 m DEM pixel size and the ~9-year time period. We
1155 computed the mean and standard deviation of the east/west (-1.5 cm/yr, 2.3 cm/yr, respectively) and north/south (-2.0 cm/yr,
1.9 cm/yr) velocity components over the stable area.

Deleted: Roualt

4.5 Validation of combined InSAR and SAR feature-tracking products

To enable direct comparison of our time series results with the DEM-derived validation data, we first masked pixels with a
cold-season coherence of <0.7 (Fig. 4). These areas contain rapid winter displacement caused by backwasting of ice cliffs,
1160 which have large signals in the DEM difference products, but we do not expect to measure with Sentinel-1 SAR observations.
We next resampled the 1-m DEM-derived products to match the 20-m grid of the Sentinel-1 SAR observations using median
resampling, then smoothed the DEM-derived products to match the SAR feature tracking resolution using a gaussian kernel
size of 7 by 7 px (~140x140 m). We computed zonal statistics (mean, standard deviation) for each velocity component
(up/down, east/west) over both the moraine dam. We also computed R^2 values between the InSAR/SAR velocity and the
1165 corresponding DEM validation component. Finally, we used the north/south component of DEM-derived velocity to assess
expected bias caused by our up/down and east/west decomposition (See “LOS Decomposition bias” section of supplementary
material for additional details).

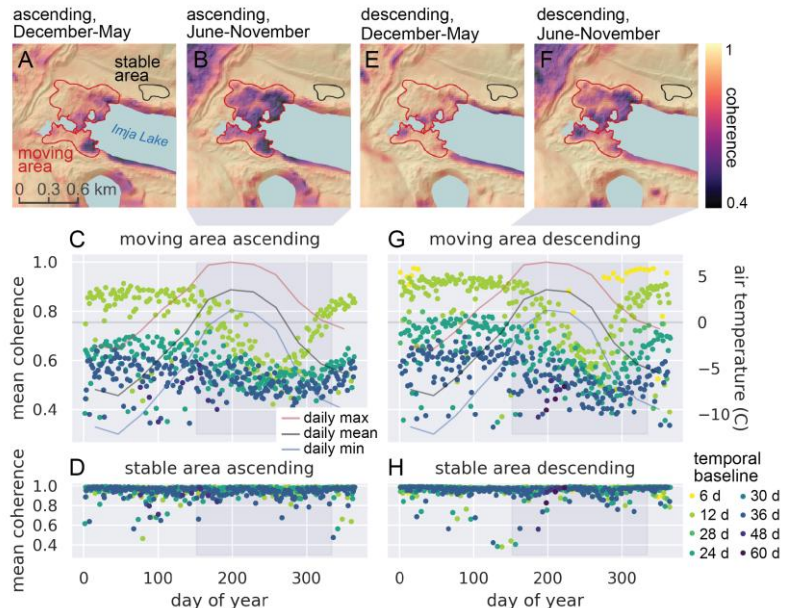
4.6 Comparison with InSAR-only and SAR-feature-tracking-only SBAS time series

We prepared two additional time series from the same Sentinel-1 SLC products: a standard InSAR-only SBAS time series and
1170 a SAR-feature-tracking-only SBAS time series. The InSAR SBAS time series used the same processing parameters as
described for our combined approach, but does not include the scaled median velocity product from feature tracking for the
inversion (blue row in Fig. 2 system of equations). The SAR-feature-tracking-only SBAS time series included the same set of
4-, 5-, and 6-year temporal baseline pairs from our combined approach (192 ascending and 210 descending), as well as all
1175 possible image pairs with a 3-year temporal baseline (182 ascending and 132 descending), to ensure that the system was
overdetermined (total ascending $n=374$, descending $n=342$). As with the DEM validation, we computed zonal statistics (mean,
standard deviation) for each velocity component (up/down, east/west) for the InSAR-only and SAR-feature-tracking-only
SBAS time series over the moraine dam.

5 Results

1180 5.1 InSAR coherence

We examined mean InSAR coherence from all pairs on both the ascending and descending orbits over the Imja Lake moraine dam during the full 2017–2024 study period. The pair temporal baseline strongly controlled InSAR coherence over the moraine dam moving area (Fig. 4E, F), with shorter temporal baselines (i.e., 12 days) offering higher mean coherence than longer temporal baselines (i.e., 36–60 days). Over the stable area, we observed no obvious relationship between temporal baseline and coherence (Fig. 4G, H). Descending orbit coherence was on average slightly higher (mean 0.80) than ascending orbit coherence (0.74) over the moraine dam moving area for 12-day temporal baseline interferograms.



1190 **Figure 4: Imja Lake moraine dam InSAR coherence and air temperature.** Mean coherence maps for all 439 12-day pairs of ascending Sentinel-1 SAR images during the colder months (A) and warmer months (B, C) Mean coherence of the moraine dam moving area in all ascending interferograms. Lines show mean daily maximum, mean, and minimum air temperature for each month from the nearby Pyramid Weather Station (UCAR/NCAR-Earth Observing Laboratory et al., 2011). D) Mean coherence of the stable area for all ascending interferograms. Panels E-H show corresponding plots for descending pairs.

Formatted: Caption

Deleted: ¶

We observed a systematic seasonal cycle in InSAR coherence values over the moraine dam moving area. Coherence remained largely stable from the beginning of the year until early June. For 12-day temporal baseline interferograms, mean coherence decreased by approximately 0.3 from June through mid-September. Coherence then increased from mid-September through

mid-November. This seasonal decrease in coherence lags about 60 days behind the timing of positive mean daily maximum temperatures at the nearby Pyramid Station (Fig. 4E, F). No significant seasonal coherence change was observed over the stable area (Fig. 4G, H).

1200 The decrease in coherence is spatially constrained. Visual inspection of mean coherence maps from the annual high-coherence period (December–May) and low-coherence period (June–November) revealed that coherence decreased over almost all of the moraine dam moving area (Fig 4A, B, C, D). Several areas of low coherence in December–May expanded and displayed a further decrease in coherence during June–November. Areas of high-coherence in December–May also displayed a decrease 1205 in coherence during June–November. Low-coherence areas were mostly consistent between ascending and descending orbits, with minor discrepancies potentially explained by differences in the LOS and acquisition time (18:00 local for ascending, 06:00 local for descending) of the two relative orbits.

1210 Applying our technique to identify and map areas of buried ice, we observed a substantial decrease (0.34) in median coherence over the moraine dam moving area between the winter to early spring (0.92) and late summer (0.58) (Fig. 5). There was no measurable decrease over the stable area.

debris-covered ice extent

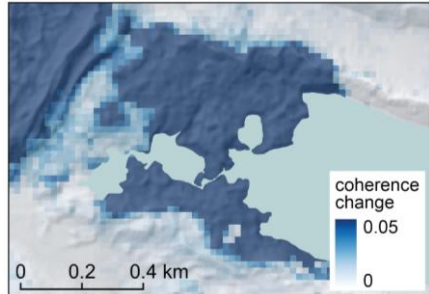
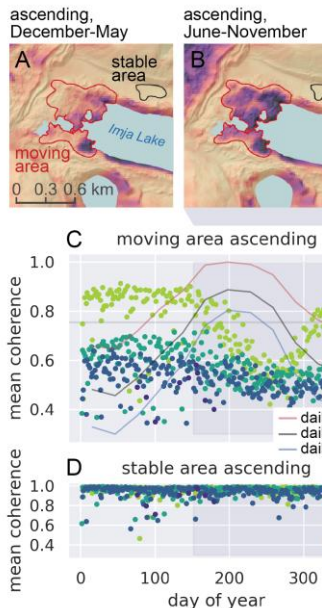


Figure 5: Seasonal change in median coherence offers a proxy to map the spatial distribution of buried ice.

5.2 Feature-tracking offset maps

1215 The feature-tracking offset maps showed coherent motion of the moraine dam surface. The spatial mean of the per-pixel median LOS velocity over the moving area was +13.6 cm/yr for the ascending orbit and +7.8 cm/yr for the descending orbit, with maximum per-pixel median LOS velocity of +46.1 cm/yr for the ascending orbit and +29.3 cm/yr for the descending orbit (Fig. 6A, B). For both orbits, higher velocity was observed on the eastern side of the moving area near the lake shoreline. The mean SNR of the feature tracking products over the moraine dam moving area was 11.4 for the ascending orbit and 14.0 for 1220 the descending orbit (Fig. 6C, D). The spatial mean of the per-pixel standard deviation of LOS velocity was 13.7 cm/yr for the



Deleted:

Figure 4: Imja Lake moraine dam InSAR coherence and air temperature. Mean coherence maps for all 439 12-day pairs of ascending Sentinel-1 SAR images during the colder months (A) and warmer months (B). C) Mean coherence of the moraine moving area in all ascending interferograms. Lines show daily maximum, mean, and minimum air temperature for each month from the nearby Pyramid Weather Station (UCAR/NCAR-Earth Observing Laboratory et al., 2011). D) Mean coherence of the stable area for all ascending interferograms. Panels E-H show corresponding plots for descending pairs. ¶

ascending orbit and 25.9 cm/yr for the descending orbit (Fig. 6E, F). The spatial mean of per-pixel median LOS velocity over the stable area was 0.7 cm/yr for the ascending track and -0.3 cm/yr for the descending track, though the feature tracking 1235 velocity values were ultimately masked in these areas with high InSAR coherence prior to inversion (Section 4.2). Positive LOS velocities are also observed over the Lhotse Glacier northwest of the moraine dam (Fig. 6A, B).

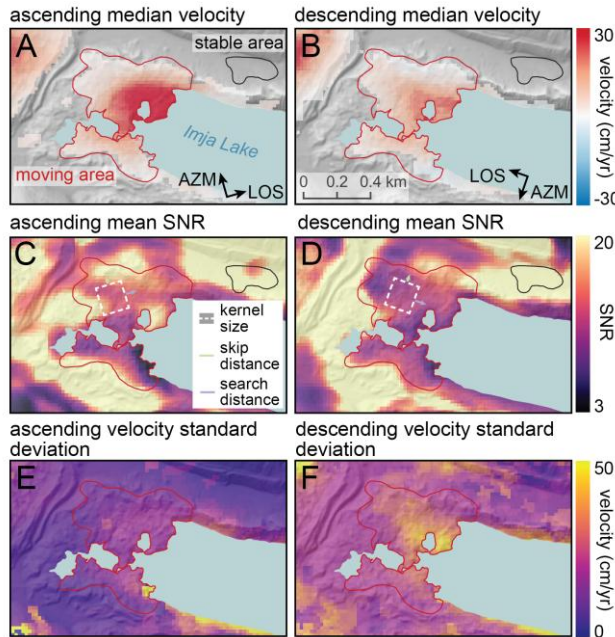
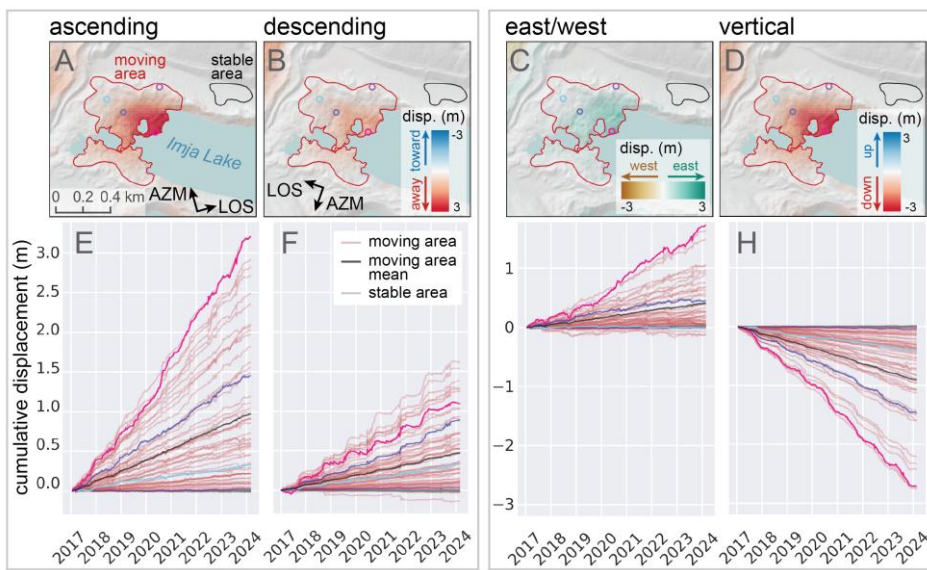


Figure 6: Sentinel-1 SAR image feature tracking results for the full 2017-2024 time series, including all 192 pairs on ascending (left) and 210 pairs on descending (right) orbits. A, B) Per-pixel median feature tracking velocity in the slant-range direction (along the line-of-sight). Results are masked in areas with high InSAR coherence (Figure 4), where feature tracking products are not used during inversion. C, D) Per-pixel median signal-to-noise (SNR) ratio. E, F) Per-pixel standard deviation of the feature tracking 1240 velocity in range direction. Higher standard deviation values are observed for locations with 1) greater temporal variability, 2) fewer reliable displacement measurements, and/or 3) larger measurement error.

5.3 Cumulative displacement time series from combined InSAR and feature tracking inversion

1245 Most pixels in the moving area showed positive range change (i.e., movement away from the satellite) over the course of the study period for both ascending and descending orbits (Fig. 7A, B). The mean total LOS displacement of the moraine dam moving area over the 7-year study period was 97.7 cm for the ascending orbit and 50.5 cm for the descending orbit, with maximum LOS displacement of 338.6 cm for the ascending orbit and 207.4 cm for the descending orbit. The largest displacements were observed on the east side of the moving area near the lake shore, while limited displacement was observed

1250 on the northern, southern, and western margins of the moving area. While many pixels displayed constant LOS velocities over time, others showed apparent seasonal fluctuations (Fig. 7E, F). To assess error caused by atmospheric noise, we first computed the mean apparent displacement in the stable area at each time step, then computed the standard deviation over all time steps. These values were 0.2 cm/yr for the ascending orbit and 0.3 cm/yr for the descending orbit, indicating that our approach for atmospheric noise removal was effective.



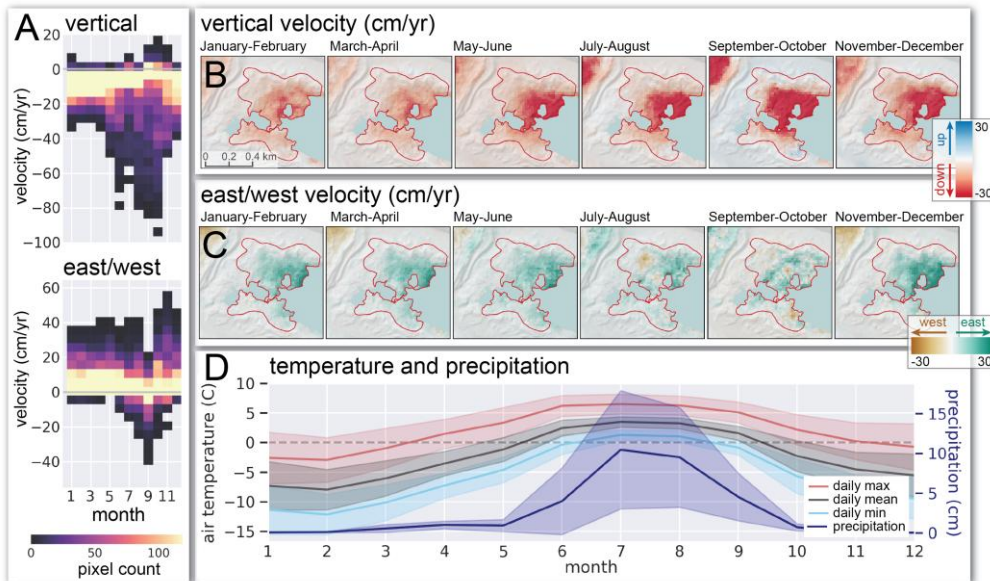
1255 **Figure 7: Cumulative displacement time series from the combined InSAR and feature tracking inversion.** A–D) Maps showing total cumulative line-of-sight (LOS) displacement of the moraine dam and stable area over the study period for the ascending (A) and descending (B) orbits, and the east/west (C) and vertical (D) directions. Colored circles show pixel locations for the 1st, 25th, 75th, and 99th percentile of cumulative ascending displacement values in the moving area. E–H) Cumulative displacement time series for 50 randomly selected pixels in the moving area (red lines) and 50 randomly-selected pixels in the stable area (grey lines). The black lines show the mean of all pixels in the moving area. The colored lines show the cumulative displacement time series for the pixels marked with corresponding colored circles in the maps.▼

Deleted: ¶
¶

1260 After decomposing the LOS displacement into vertical and east/west displacement, we found that the observed LOS displacement of the moraine dam is consistent with downward and eastward motion (Fig. 8B, C). The mean total vertical displacement of the moraine dam moving area over the study period was -93.4 cm, with a maximum total vertical displacement of -337.0 cm. The mean total eastward displacement was 38.3 cm, with a maximum displacement of 174.1 cm. Over the stable

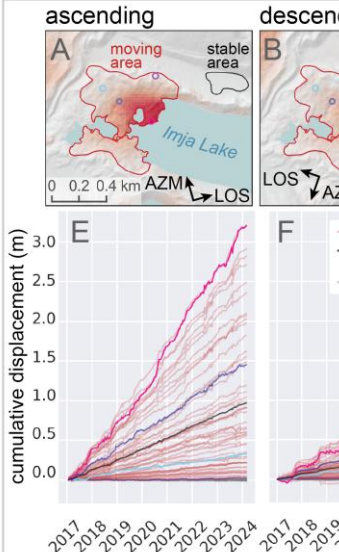
1270 area, the mean total vertical and horizontal displacement was 0.7 cm and 0.8 cm, respectively. While some pixels showed constant velocity over time, the pixels with highest velocity displayed more seasonal variability, with increased velocity during the warmer months (Fig. 7G, H).

1275 The monthly median velocity maps show year-round movement of the moraine dam with a clear seasonal cycle. Vertical velocity was lowest (between -8.6 cm/yr and -10.1 cm/yr) in January through April (Fig. 8A, B). The moraine dam moving area vertical velocity increased from May through October, when the mean vertical velocity reached -21.7 cm/yr (Fig. 8A, B). Vertical velocity over the moraine dam moving area then decreased in November and December (Fig. 8A).



1280 **Figure 8: Monthly surface velocity of the Imja Lake moraine dam from the combined InSAR and feature tracking inversion. A)** Histograms showing distribution of median monthly surface velocity values in the moving area over time. B, C) Maps showing vertical and east/west median surface velocity during bimonthly periods. D) Mean daily air temperature and precipitation for each month at the nearby Pyramid Weather Station (UCAR/NCAR-Earth Observing Laboratory et al., 2011). Shaded areas show one standard deviation.

1285 From December-May, the mean horizontal velocity of the moraine dam moving area was 6.0 to 8.3 cm/yr to the east, with limited pixel-to-pixel variability (Fig. 8A, C). Between June and September, some pixels began to move westward, and pixel-to-pixel variability increased (Fig. 8A, C). Mean east/west velocity in the moving area decreased from June through September (Fig. 8A, C).



Deleted: Figure 7: Cumulative displacement time series from the combined InSAR and feature tracking inversion. A-D) Maps showing total cumulative line-of-sight (LOS) displacement of moraine dam and stable area over the study period for the ascending (A) and descending (B) orbits, and the east/west (C) and vertical (D) directions. Colored circles show pixel location for the 1st, 25th, 75th, and 99th percentiles of cumulative ascending displacement values in the moving area. E-H) Cumulative displacement time series for 50 randomly selected pixels in the moving area (red lines) and 50 randomly selected pixels in the stable area (grey lines). The black lines show the mean of all pixels in the moving area. The colored lines show cumulative displacement time series for the pixels marked with corresponding colored circles in the maps. ¶

5.3 Validation

Our analysis shows that both the magnitude and direction of the combined InSAR and feature tracking velocity time series are consistent with the corresponding DEM validation components (Fig. 9; Table 2). The mean vertical velocity in the moving area from DEM differencing was -15.0 cm/yr. The mean vertical velocity from our combined InSAR and feature-tracking time series approach was -13.0 cm/yr. The InSAR-only SBAS underestimates both vertical and horizontal velocity. The feature-tracking-only SBAS captures velocity magnitude, but fails to capture short-term variability, and contains large errors.

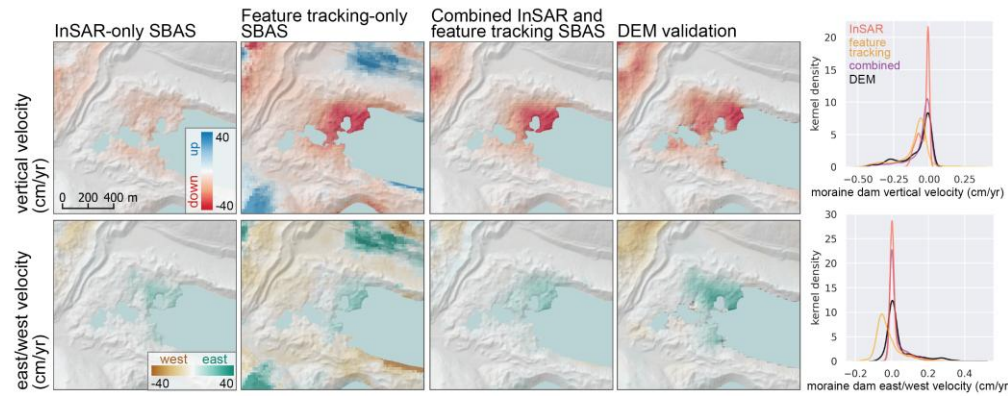


Figure 9: Mean vertical (top) and east/west (bottom) velocity products from InSAR-only SBAS (left), feature-tracking-only SBAS (left center), our combined InSAR and SAR feature tracking SBAS approach (right center), and the downsampled DEM validation data (right). Our combined approach provides the best agreement with the validation data.

Table 2. Moraine dam velocity components from InSAR-only SBAS, feature-tracking-only SBAS, our combined InSAR and feature tracking SBAS approach, and the DEM validation data. The R^2 values were computed from per-pixel differences of each approach with the corresponding DEM validation data.

	Mean (U/D)	Mean (E/W)	Std (U/D)	Std (E/W)	R^2 (U/D)	R^2 (E/W)
InSAR-only SBAS	-3.7	1.8	3.9	3.9	0.63	0.82
Feature-tracking-only SBAS	-10.2	2.0	10.6	6.9	0.67	0.35
Combined SBAS	-6.7	2.4	9.9	4.6	0.78	0.58
DEM-derived validation	-8.0	4.0	10.6	8.1	—	—

6 Discussion

Our combined InSAR and feature tracking surface displacement results can be used along with coherence change results to both infer the primary processes responsible for moraine dam degradation, and to constrain the timing and magnitude of those
1320 processes.

6.1 Ice melt

We interpret the observed seasonal decrease in coherence to be caused by melting of buried ice and associated debris reworking. The lag between the onset of air temperatures above freezing and melt onset (Fig. 4) is likely related to debris cover insulation. Melt of buried ice and debris reworking changes the moraine surface geometry, altering the scattering characteristics
1325 of the surface and decreasing coherence. ▾

Where the magnitude of the seasonal change in coherence is large (Fig. 5), we assume that buried ice is present. We find evidence for buried ice over most of the moraine dam, including areas displaying near-zero surface displacement. This is consistent with previous geophysical survey results. Hambrey et al. (2008) used both GPR and ERT to document buried glacier
1330 ice tens of meters thick (over 40 meters in places) overlain by up to 20 m of debris along the eastern portion of the moraine. Somos-Valenzuela et al., (2012) found consistent evidence for buried ice throughout 13 GPR transects across the moraine dam, ranging in bottom depth from 0–65 m. The deepest ice bottom depths (40–60 m) were documented on the northeast moraine dam, while shallower ice bottom depths (20–40 m) were documented around the southwest margin of the moraine
1335 dam, near the outlet. Dahal et al., (2018) conducted a dense ERT survey of the area surrounding the moraine dam outlet to the southwest, finding evidence for discontinuous blocks of glacier ice at depths varying from 0–20 m. Note that Hambrey et al. (2008) and Dahal et al. (2018) estimate debris thickness, but are not able to locate the bottom of the debris-covered ice, and thus present only a lower bound on ice thickness. Meanwhile Somos-Valenzuela et al. (2012) present an ice-bottom depth, but do not estimate debris thickness, resulting in only an upper bound on ice thickness. We observe a smaller seasonal change in coherence over the southwest corner of the dam near the outlet (Fig. 5), which is consistent with the isolated ice deposits
1340 mapped by Dahal et al., (2018). The magnitude of observed seasonal coherence change is likely also related to overlying debris thickness, as thicker debris 1) provides more insulation, suppressing melt and 2) experiences less surface change per volume of ice melt at depth.

While other processes could also contribute to decreased coherence during warmer months, we did not observe loss of coherence over the stable area during the warmer months (Fig. 4G, H). This suggests that seasonal melt of massive, buried ice is primarily responsible for the observed coherence loss over the moraine dam.

Deleted: Backwasting and thermokarst development should also lead to large coherence decreases.

Deleted: O

Deleted: . Exposure of interstitial ice and snow in the upper debris layer could cause a decrease in coherence. Meltwater from massive or interstitial ice may further cause changes in surface water distribution and soil moisture, contributing to decreased coherence (e.g., Lu & Meyer, 2002; Nolan et al., 2003). Increased summer precipitation (Fig. 8D) can also affect surface water and soil moisture. Changes in surface water and soil moisture driven by summer precipitation are expected to impact the dielectric properties of the moraine dam and the nearby stable area similarly. Surface snow and interstitial ice in the upper debris layer may also be present over both the stable area and the moraine dam. However,

Deleted: no

Deleted: was observed

Deleted: ,

Deleted: ing

The observed spatial variability in seasonal coherence change may be explained by debris thickness and proximity to the lake and surface ponds, which can enhance downwasting and backwasting (Johnson, 1971; Driscoll, 1980; Pickard, 1983; Watanabe et al., 1995). Low coherence during colder months was observed in some locations, especially bordering the lake and surface ponds (Fig. 2A, C). These areas tend to coincide with areas experiencing rapid subsidence in our DEM validation data (Fig. 1370 3). When air temperatures are below freezing, these locations potentially experience additional ice degradation and associated debris reworking due to melt caused by contact with water and by calving.

Overall, our measured vertical velocity values (Fig. 8) are lower than those documented by earlier studies. Watanabe et al. (1995) measured the position of five painted boulders in November 1989 and October 1994 and documented cumulative 1375 vertical displacements of -0.3 to -13.5 m with a mean of -4.8 m over the 5-year period (corresponding to vertical velocity range of -0.06 to -2.70 m/yr, and mean of -1.0 m/yr). Fujita et al. (2009) performed topographic surveys using a theodolite in November 2001 and GPS receivers in April 2002 and October 2007. They created digital elevation models (DEMs) with 1 m posting for each survey and differenced to estimate cumulative vertical surface displacement. They report cumulative vertical displacement values for the “left bank” and “right bank” of -1.63 ± 1.71 m and -1.97 ± 1.67 m (mean \pm 1-sigma), respectively, 1380 with a total range of vertical velocity values over the moraine dam of -0.06 to -1.03 m/yr for the 6-year period from 2001 to 2007. Haritashya et al. (2018) measured mean vertical velocity over the moraine dam between February 2000 and February 2016 of less than -0.5 m/yr, with a maximum of -1.9 m/yr, and uncertainty of 0.7 m/yr. The disagreement with our measured vertical velocity values (Fig. 8, Table 2) likely results from some combination of inaccurate and/or incomplete sampling of the moraine dam surface in previous work and a real decrease in the moraine dam vertical velocity over time.

1385

During the warmer months, we observed a clear increase in downward vertical velocity over much of the moraine dam (Fig. 8A, B), likely associated with melting of buried ice. The highest downward velocity over the moving area was observed in October with mean velocity of -21 cm/yr. Increases in velocity were first observed over the northern margin of the lake and surface ponds, suggesting earlier seasonal melt in these locations. Small areas of apparent upward displacement at the southern 1390 margin of the lake (Fig. 8B) are likely caused by consistent unwrapping errors due to low coherence (Fig. 4B, D). East-west displacement during the warmer months was variable, with some areas mostly moving east and some areas mostly moving west (Fig. 8C). This variability in horizontal displacement direction could be caused by the variable topography of the moraine dam, as the apparent direction of displacement caused by melt of sloped ice surfaces depends on the aspect of the surface.

1395

If we extrapolate the observed 2017 to 2024 mean subsidence rates forward in time, and consider the current moraine dam topography (Fig. S1), we find that the northeast area of the moraine dam bordering the lake edge is most vulnerable to subsidence below the current lake level. This topographic evolution would result in westward expansion of Imja Lake, decreasing the width of the moraine dam.

6.2 Ice flow

1400 During the colder months, we observed widespread downward and eastward displacement of the moraine dam surface, with a mean velocity within the moving area of -10.5 and 7.3 cm/yr, respectively (Fig. 8). The high coherence values over the moraine dam during colder months (Fig. 4) provide high confidence in these measurements. Assuming that air temperatures during this period were mostly below freezing (Fig. 4D), we do not attribute this displacement to melt of buried ice. While debris settling and frost creep could potentially explain some component of downward and horizontal motion, they are not expected to cause
1405 displacement of this magnitude on these time scales (Colman & Pierce, 1986; Bursik, 1991; Hallet & Putkonen, 1994) and we do not observe similar motion over debris outside the moraine dam. We instead attribute this motion primarily to flow of the thick, massive ice within the moraine dam.

1410 Downward and eastward movement is consistent with along-slope flow for the broad moraine dam slopes (Fig. S1). The mean surface slope of the moving area is 9.5°. Somos-Valenzuela et al. (2012) found evidence for ice bottom depths between 30 and 60 m over much of the moraine dam. Assuming debris thickness of less than 1–20 m (Hambrey et al., 2008), buried ice in the moraine dam should have thickness between 10 and 60 m. We generally observe higher east/west and vertical surface velocity during colder months over areas with deeper ice bottom depths documented by earlier studies. Near-zero velocity was observed over the southwest portion of the moraine dam, where Dahal et al. (2018) observed discontinuous blocks of buried ice. The
1415 observed mean winter velocity magnitude (combining the vertical and east/west components) of 12.8 cm/yr over the moving area of the moraine dam is consistent with expected surface velocity values for a simple ice flow model and the range of measured ice thickness (See supplementary Section S2, Fig. S9).

1420 Previous surface displacement measurements also provide evidence for flow of buried ice within the moraine dam. Watanabe et al. (1995) described westward movement of several boulders along the outlet channel of -0.96 m/yr. Fujita et al., (2009) described horizontal flow rates of less than 0.17 m/yr in an unspecified direction. Our results suggest that at some point the flow direction evolved from westward, downvalley flow (the original flow direction of Imja Glacier) to the eastward, upvalley flow (toward Imja Lake) observed during our 2017–2024 study period.

1425 The observed change in flow direction is likely related to evolving thickness of lower Imja Glacier through differential ablation both above and below the lake surface (Kjær & Krüger, 2001), changing longitudinal stresses associated with decoupling from the active flowing glacier during retreat, and interaction with the expanding lake. We observe a concave-upward transverse profile (bottom right panel of Fig. S10) for the Imja Lake moraine dam. A similar configuration, where the glacier surface slopes downward from the lateral and terminal moraines toward the centerline, is observed for a number of debris-covered
1430 glaciers in the Everest region (e.g., Nuptse Glacier, Fig. S11). This scenario introduces driving stress toward the glacier centerline (downslope), which is consistent with observed motion in our horizontal surface velocity maps. Our detailed

Deleted: ¶

Deleted: ¶

¶ We hypothesize that this morphology is likely the result of differential ablation caused by some combination of spatially variable debris thickness and local topographic shading from large lateral moraines. At the Imja Lake moraine dam, the topographic inversion may be accelerated by enhanced ablation of exposed ice at the lake edge. In addition, the buried ice in the moraine dam is no longer under the compressive longitudinal stress regime experienced when previously connected to the actively flowing main glacier. Some portion of the eastward, downslope flow could be related to the evolving longitudinal stress. To assess timescales for development of this concave-up morphology, we looked for evidence of long-wavelength slope and aspect change between the Shuttle Radar Topography Mission (SRTM) DEM acquired in February 2000 and modern WorldView DEMs (2016 and 2025). found that the moraine dam slope and aspect has not changed substantially since 2000. Given limited observational data, we are unable to constrain the timing of the transition from mostly westward to mostly eastward moraine dam surface movement.

displacement time series can be used to constrain ice and debris evolution models, which are needed to better understand the Imja Lake moraine dam evolution and implications for changing structural stability.

2285 **6.3 Limitations**

While our InSAR and feature tracking results improve our understanding of the processes responsible for moraine dam degradation, it is important to discuss some limitations. Underestimation of rapid, localized surface displacement can partly explain why our maximum vertical velocity over the moraine dam surface was only -0.47 m/yr compared to -1.9 m/yr from Haritashya et al. (2018). We also see evidence of localized backwasting in our DEM validation dataset (Fig. 3) that are not 2290 captured in our InSAR and feature-tracking displacement time series (Fig. 7, 8).

We also acknowledge limitations of the Sentinel-1 acquisition geometry, with only ~10% of any real north-south displacement mapped into LOS measurements for this location. We combined data from ascending and descending passes to calculate east/west and vertical displacement, assuming that north/south displacement does not substantially contribute to the 2295 displacement observations. In fact, some small contribution from north/south displacement is expected, which potentially introduces a source of error in our measurements of surface velocity (Brouwer & Hanssen, 2021). Based on the north/south displacement from the DEM validation dataset, we expect that our LOS decomposition could introduce a bias of ~4% in mean vertical velocity over the moraine dam moving area and ~3% in mean east/west velocity over the moraine dam moving area (Section S2, Fig. S12, S13).

2300 **7 Conclusions**

We demonstrated that Sentinel-1 InSAR and SAR feature tracking can be used to measure displacement of an ice-cored moraine dam bounding Imja Lake in Nepal. We validated our measurements using a high-resolution 3D displacement dataset from stereo DEMs. By combining InSAR and feature tracking measurements, we created a surface displacement time series that is more accurate than using InSAR or feature tracking alone. We find that a 0.3 km² area of the moraine dam subsided an 2305 average of ~90 cm over the 7-year study period, and the northeast area of the moraine dam bordering the lake edge is most vulnerable to subsidence below the current lake level.

We observed a systematic seasonal cycle in InSAR coherence values over the moraine dam surface, with a substantial decrease in coherence occurring about 60 days after mean daily maximum air temperatures rise above 0°C. We showed that seasonal changes in InSAR coherence can be used to map buried ice within the moraine dam, with an observed spatial distribution that 2310 is consistent with previous geophysical surveys.

Our results suggest that the primary processes contributing to moraine dam degradation are buried ice melt and ice flow. Buried ice melt occurs in the summer and fall, resulting in a seasonal increase in downward vertical velocity (from about -9 to -21

cm/yr on average) and variable horizontal velocity over the surface of the moraine dam. Ice flow occurs year-round and results mostly in eastward movement. Our surface velocity measurements, alongside historical measurements, provide evidence that
2315 the Imja Lake moraine dam is undergoing kinematic changes which we attribute to changing ice thickness, past decoupling from the Imja Glacier, and interaction with Imja Lake.

Collectively, our findings demonstrate the potential for SAR remote sensing to quantify the evolution of moraine dam degradation and provide new information about moraine dam internal structure. This information may be valuable when assessing GLOF hazards, performing in-situ investigations, and planning hazard remediation activities. We are extending this
2320 analysis to other high-priority moraine dams in the region and hope to integrate additional remote sensing measurements of surface change (e.g., NISAR, optical feature tracking).

Code availability

All source code and documentation is available on Github. The fufiters repository (<https://github.com/relativeorbit/fufiters>) contains code and documentation for reproducible data processing, and the fufiters_imja_analysis
2325 (https://github.com/gbrencher/fufiters_imja_analysis) repository contains code for data analysis and figure preparation.

Data Availability

All Sentinel-1 data are freely available from the Alaska Satellite Facility (ASF) Distributed Active Archive Center (DAAC).

Author Contribution

GB conceptualized this work with input from DS. GB and SH designed the methodology and developed the software. DS
2330 prepared the validation dataset. GB performed the analysis and prepared the manuscript with substantial input from DS and SH.

Competing Interests

The authors declare that they have no conflict of interest.

Acknowledgements

2335 GB was supported by NSF GRFP DGe-2140004. Analysis was performed using CryoCloud (NASA grants 80NSSC22K1877, 80NSSC23K0002). DS was supported by NASA awards 80NSSC20K1595 and 80NSSC24K1633. SH was supported by NSF award 2117834 and NASA award 80NSSC22K0345.

References

Ali Badal, L.: Indian soldier's body found in Teesta handed over to BSF, Dhaka Tribune, 2340 <https://www.dhakatribune.com/bangladesh/nation/327225/indian-soldier%20%99s-body-found-in-teesta-handed-over>, 6 October 2023.

Allen, S. K., Linsbauer, A., Randhawa, S. S., Huggel, C., Rana, P., and Kumari, A.: Glacial lake outburst flood risk in Himachal Pradesh, India: An integrative and anticipatory approach considering current and future threats, *Natural Hazards*, 84(3), 1741–1763, <https://doi.org/10.1007/s11069-016-2511-x>, 2016.

2345 Altena, B., Scambos, T., Fahnestock, M., and Kääb, A.: Extracting recent short-term glacier velocity evolution over southern Alaska and the Yukon from a large collection of Landsat data, *Cryosphere*, 13(3), 795–814, <https://doi.org/10.5194/tc-13-795-2019>, 2019.

Bekaert, D. P. S., Walters, R. J., Wright, T. J., Hooper, A. J., and Parker, D. J.: Statistical comparison of InSAR tropospheric correction techniques, *Remote Sensing of Environment*, 170, 40–47, <https://doi.org/10.1016/j.rse.2015.08.035>, 2015.

2350 Berardino, P., Fornaro, G., Lanari, R., and Sansosti, E.: A new algorithm for surface deformation monitoring based on small baseline differential SAR interferograms, *IEEE Transactions on geoscience and remote sensing*, 40(11), 2375–2383, <https://doi.org/10.1109/TGRS.2002.803792>, 2002.

Bertone, A., Barboux, C., Bodin, X., Bolch, T., Brardinoni, F., Caduff, R., Christiansen, H. H., Darrow, M. M., Delaloye, R., Etzelmüller, B., Humlum, O., Lambiel, C., Lilleøren, K. S., Mair, V., Pellegrinon, G., Rouyet, L., Ruiz, L., and Strozzi, T.: Incorporating InSAR kinematics into rock glacier inventories: Insights from 11 regions worldwide, *The Cryosphere*, 16(7), 2769–2792, <https://doi.org/10.5194/tc-16-2769-2022>, 2022.

Beyer, R. A., Alexandrov, O., and McMichael, S.: The Ames Stereo Pipeline: NASA's open source software for deriving and processing terrain data. *Earth and Space Science*, 5(9), 537–548, <https://doi.org/10.1029/2018EA000409>, 2018.

Bontemps, N., Lacroix, P., and Doin, M. P.: Inversion of deformation fields time-series from optical images, and application 2360 to the long term kinematics of slow-moving landslides in Peru, *Remote sensing of environment*, 210, 144–158, <https://doi.org/10.1016/j.rse.2018.02.023>, 2018.

Brouwer, W. S., and Hanssen, R. F.: An Analysis of InSAR Displacement Vector Decomposition Fallacies and the Strap-Down Solution, 2021 IEEE International Geoscience and Remote Sensing Symposium IGARSS, 2927–2930. <https://doi.org/10.1109/IGARSS47720.2021.9554216>, 2021.

Deleted: Bartholomew, I., Nienow, P., Mair, D., Hubbard, A., King, M. A., and Sole, A.: Seasonal evolution of subglacial drainage and acceleration in a Greenland outlet glacier, *Nature Geoscience*, 3(6), 408–411, <https://doi.org/10.1038/ngeo863>, 2010. ¶
Schmidt, D.: Deformation responses of slow moving landslides to seasonal rainfall in the Northern Apennines, measured by InSAR, *Geomorphology*, 308, 293–306, <https://doi.org/10.1016/j.geomorph.2018.02.020>, 2018. ¶

Budhathoki, K. P., Bajracharya, O., and Pokharel, B.: Assessment of Imja Glacier Lake outburst Flood (GLOF) Risk in Dudh
2375 Koshi River Basin using Remote Sensing Techniques, *Journal of Hydrology and Meteorology*, 7(1), 75–91.
<https://doi.org/10.3126/jhm.v7i1.5618>, 1970.

Bürgmann, R., Rosen, P. A., and Fielding, E. J.: Synthetic Aperture Radar Interferometry to Measure Earth's Surface
Topography and Its Deformation, *Annual Review of Earth and Planetary Sciences*, 28(1), 169–209,
<https://doi.org/10.1146/annurev.earth.28.1.169>, 2000.

2380 Bursik, M.: Relative Dating of Moraines Based on Landform Degradation, Lee Vining Canyon, California, *Quaternary
Research*, 35(3-Part1), 451–455. [https://doi.org/10.1016/0033-5894\(91\)90057-C](https://doi.org/10.1016/0033-5894(91)90057-C), 1991.

Bhushan, S., and Shean, D.: Chamoli Disaster Pre-event 2-m DEM Composite: September 2015 (1.0) [data set], Zenodo,
<https://doi.org/10.5281/zenodo.4554647>, 2021.

Bhushan, S. and Shean, D.: uw-cryo/debris_cover_smb: Bugfix for disp_mgm_corr.py (0.4.1) [code], Zenodo.
2385 <https://doi.org/10.5281/zenodo.14816790>, 2025.

Bhushan, S., Shean, D., Hu, J. Y. M., Guillet, G., and Rounce, D. R.: Deriving seasonal and annual surface mass balance for
debris-covered glaciers from flow-corrected satellite stereo DEM time series. *Journal of Glaciology*, 70, e6,
doi:10.1017/jog.2024.57, 2024.

2390 Cabré, A., Remy, D., Aguilar, G., Carretier, S., and Riquelme, R.: Mapping rainstorm erosion associated with an individual
storm from InSAR coherence loss validated by field evidence for the Atacama Desert. *Earth Surface Processes and
Landforms*, 45(9), 2091–2106, <https://doi.org/10.1002/esp.4868>, 2020.

Carrivick, J. L., & Tweed, F. S.: A global assessment of the societal impacts of glacier outburst floods, *Global and Planetary
Change*, 144, 1–16, <https://doi.org/10.1016/j.gloplacha.2016.07.001>, 2016.

2395 Casu, F., Manconi, A., Pepe, A., and Lanari, R.: Deformation time-series generation in areas characterized by large
displacement dynamics: The SAR amplitude pixel-offset SBAS technique, *IEEE Transactions on Geoscience and
Remote Sensing*, 49(7), 2752–2763, 2011.

Chini, M., Pelich, R., Pulvirenti, L., Pierdicca, N., Hostache, R., and Matgen, P.: Sentinel-1 InSAR Coherence to Detect
Floodwater in Urban Areas: Houston and Hurricane Harvey as A Test Case, *Remote Sensing*, 11(2), Article 2,
<https://doi.org/10.3390/rs11020107>, 2019.

2400 Choudhury, S. N., and Hussain, Z.: Floods in India's Sikkim state leave 10 dead, 82 missing, *Reuters*,
<https://www.reuters.com/world/india/nearly-two-dozen-indian-troops-missing-after-flash-flood-ani-2023-10-04/>, 5
October 2023.

Colman, S. M., and Pierce, K. L.: Glacial Sequence Near McCall, Idaho: Weathering Rinds, Soil Development, Morphology,
and Other Relative-Age Criteria, *Quaternary Research*, 25(1), 25–42, [https://doi.org/10.1016/0033-5894\(86\)90041-4](https://doi.org/10.1016/0033-5894(86)90041-4), 1986.

2405 Cuffey, K.M., & Paterson, W.S.B.: *The Physics of Glaciers (Fourth Edition)*, Butterworth-Heinemann, 2010.

Deleted: Cicoira, A., Beutel, J., Failletaz, J., and Vieli, A.: Water controls the seasonal rhythm of rock glacier flow, *Earth and Planetary Science Letters*, 528, 115844, <https://doi.org/10.1016/j.epsl.2019.115844>, 2019.¶

Deleted: Costa, J. E., and Schuster, R. L.: The formation and failure of natural dams, *GSA Bulletin*, 100(7), 1054–1068, [https://doi.org/10.1130/0016-7606\(1988\)100<1054:TAFON>2.3.CO;2](https://doi.org/10.1130/0016-7606(1988)100<1054:TAFON>2.3.CO;2), 1988.¶

Deleted: . (2010)

Deleted: .

Deleted: .

Dahal, P., Paudyal, K., & Rajaure, S.: Geophysical study on moraine dam of Imja Glacial Lake in Eastern Nepal using Electrical Resistivity Tomography Method, Journal of Nepal Geological Society, 55, 15–22, 2420 <https://doi.org/10.3126/jngs.v55i1.22784>, 2018.

Driscoll, F. G.: Wastage of the Klutlan Ice-Cored Moraines, Yukon Territory, Canada, Quaternary Research, 14(1), 31–49, [https://doi.org/10.1016/0033-5894\(80\)90005-8](https://doi.org/10.1016/0033-5894(80)90005-8), 1980.

Emmer, A., and Cochachin, A. The causes and mechanisms of moraine-dammed lake failures in the Cordillera Blanca, North American Cordillera, and Himalayas, AUC GEOGRAPHICA, 48(2), 5–15, 2425 <https://doi.org/10.14712/23361980.2014.23>, 2013.

Emmer, A., Vilimek, V., and Zapata, M. I.: Hazard mitigation of glacial lake outburst floods in the Cordillera Blanca (Peru): The effectiveness of remedial works, Journal of Flood Risk Management, 11(S1), S489–S501, 2425 <https://doi.org/10.1111/jfr3.12241>, 2018.

Euillardes, L. D., Euillardes, P. A., Riveros, N. C., Masiokas, M. H., Ruiz, L., Pitte, P., ... and Balbarani, S.: Detection of glaciers 2430 displacement time-series using SAR, Remote sensing of Environment, 184, 188–198, <https://doi.org/10.1016/j.rse.2016.07.003>, 2016.

European Space Agency.: Copernicus Digital Elevation Model (DEM) [Computer software], <https://registry.opendata.aws/copernicus-dem/>, 2021.

European Space Agency.: Copernicus DEM Product Handbook (v4.0) [Computer software], 2435 https://spacedata.copernicus.eu/documents/20123/121239/GEO1988-CopernicusDEM-SPE-002_ProductHandbook_I4.0.pdf/92df0801-6714-20e4-75ae-0be634b9e301?t=1666775307957, 2022.

Fahnstock, M., Bindschadler, R., Kwok, R., and Jezek, K. Greenland Ice Sheet Surface Properties and Ice Dynamics from ERS-1 SAR Imagery, Science, 262(5139), 1530–1534, <https://doi.org/10.1126/science.262.5139.1530>, 1993.

Fahnstock, M., Scambos, T., Moon, T., Gardner, A., Haran, T., and Klinger, M. Rapid large-area mapping of ice flow using 2440 Landsat 8, Remote Sensing of Environment, 185, 84–94, <https://doi.org/10.1016/j.rse.2015.11.023>, 2016.

Fuhrmann, T., and Garthwaite, M. C. Resolving Three-Dimensional Surface Motion with InSAR: Constraints from Multi-Geometry Data Fusion, Remote Sensing, 11(3), Article 3, <https://doi.org/10.3390/rs11030241>, 2019.

Fujita, K., Sakai, A., Nuimura, T., Yamaguchi, S., and Sharma, R. R.: Recent changes in Imja Glacial Lake and its damming 2445 moraine in the Nepal Himalaya revealed by in situ surveys and multi-temporal ASTER imagery, Environmental Research Letters, 4(4), 045205, <https://doi.org/10.1088/1748-9326/4/4/045205>, 2009.

Fujita, K., Sakai, A., Takenaka, S., Nuimura, T., Surazakov, A. B., Sawagaki, T., and Yamanokuchi, T.: Potential flood volume of Himalayan glacial lakes, Natural Hazards and Earth System Sciences, 13(7), 1827–1839, <https://doi.org/10.5194/nhess-13-1827-2013>, 2013.

Gray, L., Joughin, I., Tulaczyk, S., Spikes, V.B., Bindschadler, R., and Jezek, K.: Evidence for subglacial water transport in 2450 the West Antarctic Ice Sheet through three-dimensional satellite radar interferometry, Geophysical Research Letters, 32(3), <https://doi.org/10.1029/2004GL021387>, 2005.

Deleted: Etzelmüller, B.: Quantification of thermo-erosion pro-glacial areas-examples from Svalbard, Zeitschrift für Geomorphologie, 343–361, <https://doi.org/10.1127/zfg/44/2000/343>, 2000.¶

Guo, L., Li, J., Li, Z. W., Wu, L. X., Li, X., Hu, J., ... and Li, Z. Q.: The surge of the Hispar Glacier, Central Karakoram: SAR 3-D flow velocity time series and thickness changes, *Journal of Geophysical Research: Solid Earth*, 125(7), e2019JB018945, <https://doi.org/10.1029/2019JB018945>, 2020.

Gupta, V., Rakkasagi, S., Rajpoot, S., Imanni, H. S. E., and Singh, S.: Spatiotemporal analysis of Imja Lake to estimate the 2460 downstream flood hazard using the SHIVEK approach. *Acta Geophysica*, 71(5), 2233-2244, <https://doi.org/10.1007/s11600-023-01124-2>, 2023.

Hallet, B., and Putkonen, J.: Surface Dating of Dynamic Landforms: Young Boulders on Aging Moraines, *Science*, 265(5174), 937-940, <https://doi.org/10.1126/science.265.5174.937>, 1994.

Hambrey, M. J., Quincey, D. J., Glasser, N. F., Reynolds, J. M., Richardson, S. J., and Clemmens, S.: Sedimentological, 2465 geomorphological and dynamic context of debris-mantled glaciers, Mount Everest (Sagarmatha) region, Nepal, *Quaternary Science Reviews*, 27(25), 2361-2389, <https://doi.org/10.1016/j.quascirev.2008.08.010>, 2008.

Handwerger, A. L., Roering, J. J., Schmidt, D. A., and Rempel, A. W.: Kinematics of earthflows in the Northern California Coast Ranges using satellite interferometry, *Geomorphology*, 246, 321-333, <https://doi.org/10.1016/j.geomorph.2015.06.003>, 2015.

Hanssen, R. F.: *Radar Interferometry: Data Interpretation and Error Analysis*, Kluwer Academic Pub, Dordrecht, Netherlands, 2470 2001.

Haritashya, U. K., Kargel, J. S., Shugar, D. H., Leonard, G. J., Stratton, K., Watson, C. S., ... and Regmi, D.: Evolution and controls of large glacial lakes in the Nepal Himalaya, *Remote Sensing*, 10(5), 798, <https://doi.org/10.3390/rs10050798>, 2018.

Hock, R., Bliss, A., Marzeion, B., Giesen, R. H., Hirabayashi, Y., Huss, M., Radić, V., and Slangen, A. B. A.: *GlacierMIP – A model intercomparison of global-scale glacier mass-balance models and projections*, *Journal of Glaciology*, 65(251), 453-467, <https://doi.org/10.1017/jog.2019.22>, 2019.

Huggel, C., Salzmann, N., Allen, S., Caplan-Auerbach, J., Fischer, L., Haeberli, W., Larsen, C., Schneider, D., and Wessels, 2480 R.: Recent and future warm extreme events and high-mountain slope stability, *Philosophical Transactions of the Royal Society A: Mathematical, Physical and Engineering Sciences*, 368(1919), 2435-2459, <https://doi.org/10.1098/rsta.2010.0078>, 2010.

Itoh, K.: Analysis of the phase unwrapping algorithm, *Applied Optics*, 21(14), 2470-2470, <https://doi.org/10.1364/AO.21.002470>, 1982.

Jacquemart, M., and Tiampo, K.: Leveraging time series analysis of radar coherence and normalized difference vegetation 2485 index ratios to characterize pre-failure activity of the Mud Creek landslide, California, *Natural Hazards and Earth System Sciences*, 21(2), 629-642, <https://doi.org/10.5194/nhess-21-629-2021>, 2021.

Jiang, L., Fan, X., Deng, Y., Zou, C., Feng, Z., Djukem, D. L. W., ... and Xu, Q.: Combining geophysics, remote sensing and numerical simulation to assess GLOFs: Case study of the Namulacuo Lake in the Southeastern Tibetan Plateau, *Science of The Total Environment*, 880, 163262, <https://doi.org/10.1016/j.scitotenv.2023.163262>, 2023.

Deleted: Handwerger, A. L., Fielding, E. J., Huang, M. H., Bennett, G. L., Liang, C., and Schulz, W. H.: Widespread Initiation, Reactivation, and Acceleration of Landslides in the Northern California Coast Ranges due to Extreme Rainfall, *Journal of Geophysical Research: Earth Surface*, 124(7), 1782-1797, <https://doi.org/10.1029/2019JF005035>, 2019.

Deleted: Hanisch, J., Ambarish, P., Grabs, W., Dixit, A., and Reynolds, J.: GLOF mitigation strategies—Lessons learned from studying the Thulagi Glacier Lake, Nepal, *Journal of Nepal Geological Society*, 22, <https://doi.org/10.3126/jngs.v22i0.3232>, 2000.

Deleted: Healy, T. R.: Thermokarst—A mechanism of de-icing ice-cored moraines, *Boreas*, 4(1), 19-23, <https://doi.org/10.1111/j.1502-3885.1975.tb00676.x>, 1975.

Deleted: Huggel, C., Cochachin, A., Drenkhan, F., Fluijá-Samartín, J., Frey, H., García Hernández, J., Jurt, C., Muñoz-Price, K., and Vicuña, L.: Glacier Lake 513, Peru: Lessons for early warning service development, https://doi.org/10.5167/UP_186748, 2020.

Deleted: Ikeda, A., Matsuoka, N., and Kääb, A.: Fast deformation of perennially frozen debris in a warm rock glacier in the Swiss Alps: An effect of liquid water, *Journal of Geophysical Research: Earth Surface*, 113(F1), <https://doi.org/10.1029/2007JF000859>, 2008.

Irvine-Fynn, T. D. L., Barrand, N. E., Porter, P. R., Hodson, A., and Murray, T.: Recent High-Arctic glacial sediment redistribution: A process perspective using airborne lidar, *Geomorphology*, 125(1), 27-39, <https://doi.org/10.1016/j.geomorph.2010.08.012>, 2011.

Deleted: Iverson, N. R.: Shear resistance and continuity of subglacial till: Hydrology rules, *Journal of Glaciology*, 56(200), 1104-1114, <https://doi.org/10.3189/002214311796406220>, 2010.

Johnson, P. G.: Ice Cored Moraine Formation and Degradation, Donjek Glacier, Yukon Territory, Canada, *Geografiska Annaler: Series A, Physical Geography*, 53(3–4), 198–202, <https://doi.org/10.1080/04353676.1971.11879845>, 1971.

2525 Jolivet, R., and Simons, M.: A multipixel time series analysis method accounting for ground motion, atmospheric noise, and orbital errors, *Geophysical Research Letters*, 45(4), 1814–1824, <https://doi.org/10.1002/2017GL076533>, 2018.

Joughin, I.: Ice-sheet velocity mapping: A combined interferometric and speckle-tracking approach, *Annals of Glaciology*, 34, 195–201, <https://doi.org/10.3189/172756402781817978>, 2002.

Joughin, I., Smith, B. E., and Howat, I. M.: A complete map of Greenland ice velocity derived from satellite data collected over 20 years, *Journal of Glaciology*, 64(243), 1–11, <https://doi.org/10.1017/jog.2017.73>, 2018.

2530 Kellerer-pirklbauer, A., Lieb, G. K., Avian, M., and Carrivick, J.: Climate change and rock fall events in high mountain areas: Numerous and extensive rock falls in 2007 at Mittlerer Burgstall, Central Austria, *Geografiska Annaler: Series A, Physical Geography*, 94(1), 59–78, <https://doi.org/10.1111/j.1468-0459.2011.00449.x>, 2012.

Khadra, N. S.: Nepal drains dangerous Everest lake, BBC News, <https://www.bbc.com/news/world-asia-37797559>, 31 October 2016.

2535 Kjær, K. H., and Krüger, J.: The final phase of dead-ice moraine development: Processes and sediment architecture, Kötlujökull, Iceland, *Sedimentology*, 48(5), 935–952, <https://doi.org/10.1046/j.1365-3091.2001.00402.x>, 2001.

Kumar, H., and Travelli, A.: A Calamitous Flood Shows the Dangers Lurking in Melting Glaciers, *The New York Times*, <https://www.nytimes.com/2023/10/06/world/asia/india-flood-sikkim-climate-change.html>, 6 October 2023.

2540 Lacroix, P., Araujo, G., Hollingsworth, J., and Taipe, E.: Self-entrainment motion of a slow-moving landslide inferred from Landsat-8 time series, *Journal of Geophysical Research: Earth Surface*, 124(5), 1201–1216, <https://doi.org/10.1029/2018JF004920>, 2019.

Lippl, S., Vijay, S., and Braun, M.: Automatic delineation of debris-covered glaciers using InSAR coherence derived from X-, C- and L-band radar data: A case study of Yazgyl Glacier, *Journal of Glaciology*, 64(247), 811–821, <https://doi.org/10.1017/jog.2018.70>, 2018.

2545 Liu, H., Zhao, Z., and Jezek, K. C.: Synergistic Fusion of Interferometric and Speckle-Tracking Methods for Deriving Surface Velocity From Interferometric SAR Data, *IEEE Geoscience and Remote Sensing Letters*, 4(1), 102–106, <https://doi.org/10.1109/LGRS.2006.885885>, 2007.

López-Quiroz, P., Doin, M. P., Tupin, F., Briole, P., and Nicolas, J. M.: Time series analysis of Mexico City subsidence constrained by radar interferometry, *Journal of Applied Geophysics*, 69(1), 1–15, <https://doi.org/10.1016/j.jappgeo.2009.02.006>, 2009.

2550 Massonnet, D., and Feigl, K. L.: Radar interferometry and its application to changes in the Earth's surface, *Reviews of Geophysics*, 36(4), 441–500, <https://doi.org/10.1029/97RG03139>, 1998.

Mool, P. K., Maskey, P. R., Koirala, A., Joshi, S. P., Lizong, W., Shrestha, A. B., Eriksson, M., Gurung, B., Pokharel, B., Khanal, N. R., Panthi, S., Adhikari, T., Kayastha, R. B., Ghimire, P., Thapa, R., Shrestha, B., Shrestha, S., and Shrestha, R. B.: Glacial lakes and glacial lake outburst floods in Nepal, Washington, D.C.: World Bank Group,

Deleted: Johnson, P. G.: Stagnant glacier ice, St. Elias Mountains, Yukon, *Geografiska Annaler: Series A, Physical Geography*, 74(1), 13–19, <https://doi.org/10.1080/04353676.1992.11880345>, 1992.¶

Deleted: Kenner, R., Phillips, M., Beutel, J., Hiller, M., Limpach, P., Pointner, E., and Volken, M.: Factors Controlling Velocity Variations: Short-Term, Seasonal and Multiyear Time Scales, *Ritigriben Rock Glacier, Western Swiss Alps, Permafrost and Periglacial Processes*, 28(4), 675–684, <https://doi.org/10.1002/pp.1953>, 2017.¶

Deleted: King, L., and Volk, M.: Glaziologie und Glazialmorphologie des Liefde- und Bockfjordgebietes, NW-Spitsbergen, *Zeitschrift für Geomorphologie*, 97, 145–159, 1994.¶ Contrasting geometric and dynamic evolution of lake and land terminating glaciers in the central Himalaya, *Global and Planetary Change*, 167, 46–60, <https://doi.org/10.1016/j.gloplacha.2018.05.006>, 2018.¶

Deleted: Krüger, J., and Kjær, K. H.: De-icing progression of ice-cored moraines in a humid, subpolar climate, Kötlujökull, Iceland, *The Holocene*, 10(6), 737–747, <https://doi.org/10.1191/09596830094980>, 2000.¶

Deleted: Lu, Z., and Meyer, D. J.: Study of high SAR backscattering caused by an increase of soil moisture over a sparsely vegetated area: Implications for characteristics of backscattering, *International Journal of Remote Sensing*, 23(6), 1063–1074, <https://doi.org/10.1080/01433160110040035>, 2002.¶ Lukas, S., Nicholson, L. I., Ross, F. H., and Humlum, O.: Formation, meltout processes and landscape alteration of high Arctic ice-cored moraines—Examples from Nordenskiöld Land, central Spitsbergen, *Polar Geography*, 29(3), 157–187, <https://doi.org/10.1080/789610198>, 2005.¶ Lukas, S.: Ice-cored moraines, in: *Encyclopedia of Snow, Ice and Glaciers*, edited by: Singh, V. P., Singh, P., and Haritashya, U. K., Springer, Dordrecht, The Netherlands, 616–619, https://doi.org/10.1007/978-90-481-2642-2_2011, 2011.¶

Deleted: Mattson, L. E.: Ablation on debris covered glaciers example from the Rakhoti Glacier, Punjab, Himalaya, *Intern. Assoc. Hydrol. Sci.*, 218, 289–296, 1993.¶ Mattson, L. E., and Gardner, J. S.: Mass wasting on valley-side ice-cored moraines, Boundary Glacier, Alberta, Canada, *Geografiska Annaler: Series A, Physical Geography*, 73(3–4), 123–128, <https://doi.org/10.1080/04353676.1991.11880337>, 1991.¶ Mckenzie, G. D.: Observations on a collapsing kame terrace in Glacier Bay National Monument, south-eastern Alaska, *Journal of Glaciology*, 8(54), 413–425, <https://doi.org/10.3189/S0022143000027003>, 1969.¶ Minchew, B. M., and Meyer, C. R.: Dilatation of subglacial sediments governs incipient surge motion in glaciers with deformable beds, *Proceedings of the Royal Society A: Mathematical, Physical and Engineering Sciences*, 476(2238), 20200033, <https://doi.org/10.1098/rspa.2020.0033>, 2020.¶

<https://policycommons.net/artifacts/1516291/glacial-lakes-and-glacial-lake-outburst-floods-in-nepal/2192662/>, 2011.

2610 Nie, Y., Liu, Q., Wang, J., Zhang, Y., Sheng, Y., and Liu, S. An inventory of historical glacial lake outburst floods in the Himalayas based on remote sensing observations and geomorphological analysis, *Geomorphology*, 308, 91–106, <https://doi.org/10.1016/j.geomorph.2018.02.002>, 2018.

2615 Notti, D., Davalillo, J. C., Herrera, G., and Mora, O. J. N. H.: Assessment of the performance of X-band satellite radar data for landslide mapping and monitoring: Upper Tena Valley case study, *Natural Hazards and Earth System Sciences*, 10(9), 1865–1875, <https://doi.org/10.5194/nhess-10-1865-2010>, 2010.

2620 NSDDA: Geospatial positioning accuracy standards part 3: National standard for spatial data accuracy (no. FGDC-STD-007.3-1998), 1998.

Nuth, C., & Kääb, A.: Co-registration and bias corrections of satellite elevation data sets for quantifying glacier thickness change, *The Cryosphere*, 5(1), 271–290, <https://doi.org/10.5194/tc-5-271-2011>, 2011.

2625 Ohki, M., Abe, T., Tadono, T., and Shimada, M.: Landslide detection in mountainous forest areas using polarimetry and interferometric coherence, *Earth, Planets and Space*, 72(1), 67, <https://doi.org/10.1186/s40623-020-01191-5>, 2020.

Porter, C., Howat, I., Husby, E., Noh, M.J., Khuvis, S., Danish, E., Tomko, K., Gardiner, J., Negrete, A., Yadav, B., Klassen, J., Kelleher, C., Cloutier, M., Bakker, J., Enos, J., Arnold, G., Bauer, G., and Morin, P.: EarthDEM – Strips, Version 1 [dataset], Harvard Dataverse, V1, <https://doi.org/10.7910/DVN/LHE9Q7>, 2022.

2630 Rana, B., Shrestha, A. B., Reynolds, J. M., and Aryal, R.: Hazard assessment of the Tsho Rolpa Glacier Lake and ongoing, *Journal of Nepal Geological Society*, 22, 563–570, 2000.

Ravanel, L., Duvillard, P.-A., Jaboyedoff, M., and Lambiel, C.: Recent evolution of an ice-cored moraine at the Gentianes Pass, Valais Alps, Switzerland, *Land Degradation & Development*, 29(10), 3693–3708, <https://doi.org/10.1002/ldr.3088>, 2018.

2635 Riaz, S., Ali, A., and Baig, M. N.: Increasing risk of glacial lake outburst floods as a consequence of climate change in the Himalayan region, *Jāmbā: Journal of Disaster Risk Studies*, 6(1), 7, <https://doi.org/10.4102/jamba.v6i1.110>, 2014.

Richardson, S. D., and Reynolds, J. M.: An overview of glacial hazards in the Himalayas, *Quaternary International*, 65–66, 31–47, [https://doi.org/10.1016/S1040-6182\(99\)00035-X](https://doi.org/10.1016/S1040-6182(99)00035-X), 2000.

2640 Rick, B., McGrath, D., Armstrong, W., and McCoy, S. W.: Dam type and lake location characterize ice-marginal lake area change in Alaska and NW Canada between 1984 and 2019, *The Cryosphere*, 16(1), 297–314, <https://doi.org/10.5194/tc-16-297-2022>, 2022.

Rosen, P. A., Gurrola, E., Sacco, G. F., and Zebker, H.: The InSAR scientific computing environment, *EUSAR 2012; 9th European Conference on Synthetic Aperture Radar*, 730–733, <https://ieeexplore.ieee.org/abstract/document/6217174>, 2012.

Rosen, P. A., Hensley, S., Joughin, I. R., Li, F. K., Madsen, S. N., Rodriguez, E., and Goldstein, R. M.: Synthetic aperture radar interferometry, *Proceedings of the IEEE*, 88(3), 333–382, <https://doi.org/10.1109/5.838084>, 2000.

Deleted: Neupane, R., Chen, H., and Cao, C.: Review of moraine dam failure mechanism, *Geomatics, Natural Hazards Risk*, 10(1), 1948–1966, <https://doi.org/10.1080/19475705.2019.1652210>, 2019.¶

Deleted: Niggli, L., Allen, S., Frey, H., Huggel, C., Petranka, D., Raimbekova, Z., Reynolds, J., and Wang, W.: GLOF Risk Management Experiences and Options: A Global Overview, in: *Oxford Research Encyclopedia of Natural Hazard Science*, Oxford University Press, <https://doi.org/10.1093/acrefore/9780199389407.013.540>, 2020.

Nolan, M., Fatland, D. R., and Hinzman, L.: DInSAR measurement of soil moisture, *IEEE Transactions on Geoscience and Remote Sensing*, 41(12), 2802–2813, <https://doi.org/10.1109/TGRS.2003.817211>, 2003.¶

Deleted: Østrem, G.: Ice Melting under a Thin Layer of Moraine, and the Existence of Ice Cores in Moraine Ridges, *Geografiska Annaler*, 41(4), 228–230, <https://doi.org/10.1080/20014422.1959.11907953>, 1959.¶

Østrem, G.: Problems of dating ice-cored moraines, *Geografiska Annaler: Series A, Physical Geography*, 47(1), 1–38, <https://doi.org/10.1080/04353676.1965.11879710>, 1965.¶

Deleted: a

Deleted: Richardson, S. D., and Reynolds, J. M.: Degradation of ice-cored moraine dams: Implications for hazard development, *IAHS Publication*, 264, 2000b.¶

2670 Rouault, E., Warmerdam, F., Schwehr, K., Kiselev, A., Butler, H., Łoskot, M., Szekeres, T., Tourigny, E., Landa, M., Miara, I., Elliston, B., Chaitanya, K., Plesea, L., Morissette, D., Jolma, A., Dawson, N., Baston, D., de Stigter, C., & Miura, H.: GDAL (v3.9.3) [computer software], Zenodo, <https://doi.org/10.5281/zenodo.1392953>, 2024

2670 Rounce, D. R., Hock, R., and Shean, D. E.: Glacier mass change in High Mountain Asia through 2100 using the open-source python glacier evolution model (PyGEM), *Frontiers in Earth Science*, 7, 331, 2020.

Rounce, D. R., McKinney, D. C., Lala, J. M., Byers, A. C., and Watson, C. S.: A new remote hazard and risk assessment framework for glacial lakes in the Nepal Himalaya. *Hydrology and Earth System Sciences*, 20(9), 3455–3475, <https://doi.org/10.5194/hess-20-3455-2016>, 2016.

2675 Rounce, D. R., Watson, C. S., and McKinney, D. C.: Identification of Hazard and Risk for Glacial Lakes in the Nepal Himalaya Using Satellite Imagery from 2000–2015, *Remote Sensing*, 9(7), <https://doi.org/10.3390/rs9070654>, 2017.

Samsonov, S., Tiampo, K., and Cassotto, R. Measuring the state and temporal evolution of glaciers in Alaska and Yukon using synthetic-aperture-radar-derived (SAR-derived) 3D time series of glacier surface flow, *Cryosphere*, 15(9), <https://doi.org/10.5194/tc-15-4221-2021>, 2021.

2680 Sánchez-Gámez, P., and Navarro, F. J.: Glacier Surface Velocity Retrieval Using D-InSAR and Offset Tracking Techniques Applied to Ascending and Descending Passes of Sentinel-1 Data for Southern Ellesmere Ice Caps, Canadian Arctic, *Remote Sensing*, 9(5), <https://doi.org/10.3390/rs9050442>, 2017.

Sattar, A., Goswami, A., Kulkarni, Anil. V., Emmer, A., Haritashya, U. K., Allen, S., Frey, H., and Huggel, C.: Future Glacial Lake Outburst Flood (GLOF) hazard of the South Lhonak Lake, Sikkim Himalaya, *Geomorphology*, 388, 107783.

2685 Scapozza, C., Ambrosi, C., Cannata, M., and Strozzi, T.: Glacial lake outburst flood hazard assessment by satellite Earth observation in the Himalayas (Chomolhari area, Bhutan), *Geographica Helvetica*, 74(1), 125-139, <https://doi.org/10.5194/gh-74-125-2019>, 2019.

Schmidt, D. A., and Bürgmann, R.: Time-dependent land uplift and subsidence in the Santa Clara valley, California, from a 2690 large interferometric synthetic aperture radar data set, *Journal of Geophysical Research: Solid Earth*, 108(B9), <https://doi.org/10.1029/2002JB002267>, 2003.

Sebastian, M.: Sikkim: Race against time to save 102 missing in India floods, BBC, <https://www.bbc.com/news/business-66997995>, 5 October 2023.

2695 Shean, D. E., Alexandrov, O., Moratto, Z. M., Smith, B. E., Joughin, I. R., Porter, C., and Morin, P. An automated, open-source pipeline for mass production of digital elevation models (DEMs) from very-high-resolution commercial stereo satellite imagery, *ISPRS Journal of Photogrammetry and Remote Sensing*, 116, 101-117, <https://doi.org/10.1016/j.isprsjprs.2016.03.012>, 2016.

Shean, D., Bhushan, S., Lilien, D., Knuth, F., Schwat, E., Meyer, J., Sharp, M., & Hu, M.: dshean/demcoreg: v1.1.1 Compatibility and doc improvements (v1.1.1) [code], Zenodo, <https://doi.org/10.5281/zenodo.7730376>, 2023.

Deleted: Ross, A. B: A form and process response study of terminal ice cored ablation moraine, doctoral dissertation, University of Ottawa, Canada, 1976.¶

Deleted: Schomacker, A.: What controls dead-ice melting under different climate conditions? A discussion, *Earth-Science Reviews*, 90(3), 103–113, <https://doi.org/10.1016/j.earscirev.2008.08.003>, 2008.¶ Schomacker, A., and Kjær, K. H.: Quantification of dead-ice melting in ice-cored moraines at the high-Arctic glacier Holmstrømbreen, Svalbard, *Boreas*, 37(2), 211–225, <https://doi.org/10.1111/j.1502-3885.2007.00014.x>, 2008.¶

Shugar, D. H., Burr, A., Haritashya, U. K., Kargel, J. S., Watson, C. S., Kennedy, M. C., Bevington, A. R., Betts, R. A., Harrison, S., and Stratton, K.: Rapid worldwide growth of glacial lakes since 1990, *Nature Climate Change*, 10(10), <https://doi.org/10.1038/s41558-020-0855-4>, 2020.

2715 Shugar, D. H., and Clague, J. J.: The sedimentology and geomorphology of rock avalanche deposits on glaciers, *Sedimentology*, 58(7), 1762–1783, <https://doi.org/10.1111/j.1365-3091.2011.01238.x>, 2011.

✓ Somos-Valenzuela, M., McKinney, D. C., Byers, A. C., Voss, K., Moss, J., and McKinney, J. C.: Ground penetrating radar survey for risk reduction at Imja Lake, Nepal, Center for Research in Water Resources, University of Texas at Austin, <http://hdl.handle.net/2152/19751>, 2012.

Deleted: Somos-Valenzuela, M. A., McKinney, D. C., Byers, A. C., Rounce, D. R., and Portocarrero, C.: Modeling Mitigation Strategies for Risk Reduction at Imja Lake, Nepal, Center for Research in Water Resources, University of Texas at Austin, <http://hdl.handle.net/2152/27736>, 2013.¶

2720 Strozzi, T., Kouraev, A., Wiesmann, A., Wegmüller, U., Sharov, A., and Werner, C.: Estimation of Arctic glacier motion with satellite L-band SAR data, *Remote Sensing of Environment*, 112(3), 636–645, <https://doi.org/10.1016/j.rse.2007.06.007>, 2008.

Strozzi, T., Luckman, A., Murray, T., Wegmüller, U., and Werner, C. L.: Glacier motion estimation using SAR offset-tracking procedures, *IEEE Transactions on Geoscience and Remote Sensing*, 40(11), 2384–2391, <https://doi.org/10.1109/TGRS.2002.805079>, 2002.

2725 Sun, S., Che, T., Wang, J., Li, H., Hao, X., Wang, Z., & Wang, J.: Estimation and Analysis of Snow Water Equivalents Based on C-Band SAR Data and Field Measurements, *Arctic, Antarctic, and Alpine Research*, 47(2), 313–326, <https://doi.org/10.1657/AAAR00C-13-135>, 2015.

✓ Tough, J. A., Blacknell, D., and Quegan, S.: A statistical description of polarimetric and interferometric synthetic aperture radar data, *Proceedings of the Royal Society of London, Series A: Mathematical and Physical Sciences*, 449(1937), 567–589, <https://doi.org/10.1098/rspa.1995.0059>, 1995.

Deleted: Tonkin, T. N., Midgley, N. G., Cook, S. J., and Graham, D. J.: Ice-cored moraine degradation mapped and quantified using an unmanned aerial vehicle: a case study from polythermal glacier in Svalbard, *Geomorphology*, 258, 1–10, <https://doi.org/10.1016/j.geomorph.2015.12.019>, 2016.¶

2730 UCAR/NCAR-Earth Observing Laboratory, Vuillermoz, E., Tartari, G., Bertolani, L., & Ueno, K.: CEOP_AP: Himalayas Surface Meteorology and Radiation Data Set, Version 1.0 (1.0, p. 6 data files, 36 ancillary/documentation files, 189 MiB) [NetCDF: Network Common Data Form for CEOP (application/x-netcdf),CEOP/EOP-3 Surface Meteorology and Radiation (ASCII)], <https://doi.org/10.26023/ZZHE-8SAB-040R>, 2011.

Deleted: .

✓ UNDP, Community Based Flood and Glacial Lake Outburst Risk Reduction Project [Project Document], <https://www.undp.org/sites/g/files/zskgke326/files/migration/np/aa21b4ccde4230b2b26dda751438572149d185892d482a1cf417b3a1737ce05a.pdf>, 2012.

2740 Wang, W., Gao, Y., Iribarren Anacona, P., Lei, Y., Xiang, Y., Zhang, G., Li, S., and Lu, A.: Integrated hazard assessment of Cirenmaco glacial lake in Zhangzangbo valley, Central Himalayas, *Geomorphology*, 306, 292–305, <https://doi.org/10.1016/j.geomorph.2015.08.013>, 2018.

Wang, X., Liu, S., Ding, Y., Guo, W., Jiang, Z., Lin, J., and Han, Y.: An approach for estimating the breach probabilities of moraine-dammed lakes in the Chinese Himalayas using remote-sensing data, *Natural Hazards and Earth System Sciences*, 12(10), 3109–3122, <https://doi.org/10.5194/nhess-12-3109-2012>, 2012.

2755 Watanabe, T., Kameyama, S., and Sato, T.: Imja Glacier Dead-Ice Melt Rates and Changes in a Supra-Glacial Lake, 1989–1994, Khumbu Himal, Nepal: Danger of Lake Drainage, Mountain Research and Development, 15(4), 293–300, <https://doi.org/10.2307/3673805>, 1995.

2760 Watanabe, T., Lamsal, D., and Ives, J. D.: Evaluating the growth characteristics of a glacial lake and its degree of danger of outburst flooding: Imja Glacier, Khumbu Himal, Nepal, Norsk Geografisk Tidsskrift - Norwegian Journal of Geography, 63(4), 255–267, <https://doi.org/10.1080/00291950903368367>, 2009.

Wright, T. J., Parsons, B. E., and Lu, Z.: Toward mapping surface deformation in three dimensions using InSAR, Geophysical Research Letters, 31(1), <https://doi.org/10.1029/2003GL018827>, 2004.

Yang, L., Lu, Z., Zhao, C., Kim, J., Yang, C., Wang, B., ... and Wang, Z.: Analyzing the triggering factors of glacial lake outburst floods with SAR and optical images: a case study in Jinweng Co, Tibet, China, Landslides, 19(4), 855–864, 2022.

2765 Yang, L., Lu, Z., Ouyang, C., Zhao, C., Hu, X., and Zhang, Q.: Glacial Lake Outburst Flood Monitoring and Modeling through Integrating Multiple Remote Sensing Methods and HEC-RAS, Remote Sensing, 15(22), 5327, <https://doi.org/10.3390/rs15225327>, 2023.

Yu, Y., Li, B., Li, Y., and Jiang, W.: Retrospective Analysis of Glacial Lake Outburst Flood (GLOF) Using AI Earth InSAR and Optical Images: A Case Study of South Lhonak Lake, Sikkim, Remote Sensing, 16(13), 2307, <https://doi.org/10.3390/rs16132307>, 2024.

Yunjun, Z., Fattah, H., and Amelung, F.: Small baseline InSAR time series analysis: Unwrapping error correction and noise reduction, Computers & Geosciences, 133, 104331, <https://doi.org/10.1016/j.cageo.2019.104331>, 2019.

2770 Zhang, Z., Lin, H., Wang, M., Liu, X., Chen, Q., Wang, C., and Zhang, H.: A Review of Satellite Synthetic Aperture Radar Interferometry Applications in Permafrost Regions: Current status, challenges, and trends, IEEE Geoscience and Remote Sensing Magazine, 10(3), 93–114, <https://doi.org/10.1109/MGRS.2022.3170350>, 2022.

2775 Zheng, W., Bhushan, S., Van Wyk De Vries, M., Kochtitzky, W., Shean, D., Copland, L., Dow, C., Jones-Ivey, R., and Pérez, F.: GLAcier Feature Tracking testkit (GLAFT): A statistically and physically based framework for evaluating glacier velocity products derived from optical satellite image feature tracking, The Cryosphere, 17(9), 4063–4078, <https://doi.org/10.5194/tc-17-4063-2023>, 2023.

Deleted: 1

Zhang, T., Wang, W., and An, B.: A massive lateral moraine collapse triggered the 2023 South Lhonak Lake outburst flood Sikkim Himalayas, Landslides, 22(2), 299–311, <https://doi.org/10.1007/s10346-024-02358-x>, 2025.¶